

CHARACTERIZATION OF THE UNIVERSITY OF FLORIDA SOLAR SIMULATOR AND  
AN INVERSE SOLUTION FOR IDENTIFYING INTENSITY DISTRIBUTIONS FROM  
MULTIPLE FLUX MAPS IN CONCENTRATING SOLAR APPLICATIONS

By

BENJAMIN MARTIN ERICKSON

A THESIS PRESENTED TO THE GRADUATE SCHOOL  
OF THE UNIVERSITY OF FLORIDA IN PARTIAL FULFILLMENT  
OF THE REQUIREMENTS FOR THE DEGREE OF  
MASTER OF SCIENCE

UNIVERSITY OF FLORIDA

2012

© 2012 Benjamin Martin Erickson

To my beautiful wife to be, thank you for sticking with me through the years. I can't wait to turn the miles between us into inches.

## ACKNOWLEDGMENTS

First and foremost I would like to thank my parents for providing the opportunity and inspiration to be where I am today. I would also like to thank my fiancée for her never ending support and dedication. Her willingness to work through two more years of a long distance relationship allowed me to take this opportunity. I would like to thank Dr. Gregory Scott Duncan and Dr. Robert Palumbo for their assistance in both motivating me to further my education and opening doors at the University of Florida. I would also like to thank Dr. Jörg Petrasch for taking me on as a graduate student and working with me through the multitude of questions I asked. I would like to thank Dr. David Hahn and Dr. Raphael Haftka for being on my committee. Lastly, special thanks goes out to all of my lab mates at the Energy Park, it has been a pleasure working with you over the last two years.

# TABLE OF CONTENTS

	<u>page</u>
ACKNOWLEDGMENTS .....	4
LIST OF TABLES .....	7
LIST OF FIGURES .....	8
LIST OF OBJECTS .....	11
LIST OF ABBREVIATIONS .....	12
ABSTRACT .....	14
CHAPTER	
1 INTRODUCTION .....	16
Motivation .....	16
Literature Review .....	17
Outline .....	19
2 SOLAR SIMULATOR .....	20
Design .....	20
Frame/Cooling .....	20
Power System .....	21
Mirrors/Lamps .....	22
Installation .....	22
Focusing .....	23
Safety .....	24
Peripheral Subsystems .....	25
XY Table .....	25
Flux target .....	27
Camera and MATLAB .....	28
Data Measurement (DAQ) .....	29
3 MONTE CARLO SIMULATION .....	42
Monte Carlo Simulations .....	42
Simple Simulations .....	43
Simulator Model .....	43
2D Case for Intensity .....	44
3D Flux to Intensity .....	44
4 EXPERIMENTS .....	47

Flux Measurements .....	47
Flux Mapping .....	47
Simulator Flux Maps .....	49
<b>5 INVERSE METHOD.....</b>	<b>55</b>
Introduction .....	55
Methodology .....	56
Derivation for the general case.....	57
Two dimensional case.....	58
Circular Symmetric case.....	59
Regularization .....	61
Monte Carlo Ray Tracing.....	61
Results.....	61
Parabolic Trough .....	61
Elliptical Trough.....	63
Conclusions .....	63
Least Squares Constraints .....	64
Alternative Methods .....	64
Direct Measurement .....	64
Aperture Method.....	66
<b>6 CONCLUSIONS .....</b>	<b>75</b>
Summary .....	75
Outlook .....	76
 <b>APPEENDIX</b>	
<b>A SIMULATOR DRAWINGS .....</b>	<b>77</b>
<b>B SIMULATOR SAFETY AND STARTUP DOCUMENTATION .....</b>	<b>89</b>
<b>C PERIPHERAL SYSTEM DOCUMENTS .....</b>	<b>92</b>
<b>LIST OF REFERENCES .....</b>	<b>96</b>
<b>BIOGRAPHICAL SKETCH .....</b>	<b>100</b>

## LIST OF TABLES

<u>Table</u>		<u>page</u>
2-1	Parameters of the simulator mirrors. ....	30
2-2	Parameters of the simulator lamps. ....	30
2-3	Parameters of the camera and lens.....	30
2-4	Parameters of the DAQ modules.....	30
3-1	Parameters required to implement a ring in Vegas.....	44
5-1	Parameters of the parabolic trough. ....	66
5-2	Elliptical trough parameters .....	67

## LIST OF FIGURES

<u>Figure</u>		<u>page</u>
2-1	The frame of the simulator at the beginning of construction .....	31
2-2	The simulator from behind.....	31
2-3	The inside of one of the power transformers .....	32
2-4	Power to each lamp can be individually turned on or off at the main power box.....	32
2-5	The power rack houses a converter and transformer for each lamp assembly on the simulator .....	33
2-6	Ignition unit mounted below its corresponding mirror/lamp assembly.....	33
2-7	LabView program designed to control the lamps and read the flux sensor. ....	34
2-8	Mirror holder assemblies with coarse and fine adjustment .....	34
2-9	Schematic drawing showing a set of elliptical lamps with a single coincident focal point.....	35
2-10	A completed mirror and lamp assembly shown from the front and back .....	35
2-11	Phillip Hauter working to assemble the simulator frame .....	36
2-12	Installation of the power and cooling systems .....	36
2-13	Protective plexiglass cover for the control room windows .....	37
2-14	Two safety interlocks protecting the rear doors during operation of the simulator.....	37
2-15	Schematic floor plan of the experimental area.....	38
2-16	The safety panel.....	39
2-17	The Velmex BiSlide XY table.....	39
2-18	Screen shot of the XY table control program "COSMOS." .....	40
2-19	The flux target.....	40
2-20	The CCD camera and filter wheel.....	41
2-21	The DAQ and protection box in the simulator room .....	41

3-1	A simple disk and elliptical dish modeled in Vegas.....	45
3-2	The simulator as modeled in Vegas with 5.0 mrad reflection error and 7.5 mm bulb diameter.....	45
3-3	Target plot for the simulator modeled with 5.0 mrad reflection error and 7.5 mm bulb diameter.....	46
3-4	Flux distribution at the focal plane for varying reflection errors.....	46
4-1	The schematic drawing for the flux sensor from Vatech, Corp. ....	50
4-2	A schematic drawing of a typical flux measurement setup. ....	50
4-3	A raw and post processed image collected by the flux mapping system .....	51
4-4	Calibration curve relating pixel value to flux level .....	51
4-5	A completed flux map of lamp 7 with the sensor discoloration removed .....	52
4-6	A raw image of a reactor during experimentation showing slight spillage onto the aperture .....	52
4-7	Flux map from the simulator with lamp 5 or lamp 7 turned on .....	53
4-8	Flux map from the simulator with lamps 2 and 6 turned on .....	53
4-9	Flux map from the simulator with lamps 2, 4, 6 and 7 on illustrating saturation..	54
5-1	Flux mapping setup. ....	67
5-2	General case of a ray passing through multiple flux planes and the solution plane.....	68
5-3	Two-dimensional flux maps. ....	68
5-4	Schematic representation of the circular symmetric case.....	69
5-5	2D parabolic trough as modeled in VeGaS .....	69
5-6	Parabolic trough scaled flux distribution at multiple distances ( $z^*=z/f$ ) from the focal plane. ....	70
5-7	Scaled intensity distribution ( $I_{max}$ ) along the focal plane of a 2D parabolic trough from Monte Carlo ray tracing. ....	70
5-8	Scaled inverse solution results ( $I_{max}$ ) at the focal plane .....	71

5-9	Schematic representation of the elliptical trough setup as implemented in Vegas. ....	71
5-10	Scaled flux distribution at varying distances ( $z^*=z/((a+b)/2)$ ) from the parabolic trough.....	72
5-11	Scaled intensity distribution along the focal plane of a 2D parabolic trough from Monte Carlo ray tracing. ....	72
5-12	Scaled inverse solution results ( $I_{max}$ ) at the focal plane .....	73
5-13	Camera as an intensity measurement device.....	73
5-14	Schematic diagram showing a potential setup for implementing the aperture method. ....	74

## LIST OF OBJECTS

<u>Object</u>	<u>page</u>
2-1 The XY table user manual .....	29
2-2 The XY table extended user manual .....	29
2-3 Extra information pertaining to the XY table .....	29
2-4 XY table control (VXM) user manual .....	29
2-5 CCD camera user's manual.....	29
2-6 General information about the CCD camera.....	29
2-7 Supplementary information about the CCD camera .....	29
2-8 Source code for the flux mapping software.....	29
2-9 Function findminmax necessary to run flux.m.....	29
3-1 User's manual for the Monte Carlo ray tracing program Vegas .....	44

## LIST OF ABBREVIATIONS

$I(x, y, z, \theta, \varphi)$	Intensity at point $(x,y,z)$ in the direction $(\theta, \varphi)$
$I_o(x, y, \theta, \varphi)$	Intensity on the solution plane at point $(x,y)$ in the direction $(\theta, \varphi)$
$q''(x, y, z)$	Radiative flux at the point $(x,y,z)$
$q''_{jkl}$	Radiative flux at the point corresponding to $(x_j, y_k, z_l)$
$r_j$	Radial position at the $j^{\text{th}}$ discretization
$x_j$	X-position at the $j^{\text{th}}$ discretization
$x_{o,jklmn}$	X-position projected onto the solution plane corresponding to a point $(x_j, y_k, z_l)$ and direction $(\theta, \varphi)$
$y_k$	Y-position at the $k^{\text{th}}$ discretization
$y_{o,jklmn}$	Y-position projected onto the solution plane corresponding to a point $(x_j, y_k, z_l)$ and direction $(\theta, \varphi)$
$w_x$	Weighting factor in the x-direction
$w_y$	Weighting factor in the y-direction
$w_r$	Weighting factor in the r-direction
$w_\theta$	Weighting factor in the $\theta$ -direction
$w_\varphi$	Weighting factor in the $\varphi$ -direction
$z_l$	Z-position at the $l^{\text{th}}$ discretization
$\Delta x$	Bin size in the x-direction
$\Delta y$	Bin size in the y-direction
$\Delta z$	Distance between planes in the z-direction
$\Delta \theta$	Bin size in the $\theta$ -direction
$\Delta \varphi$	Bin size in the $\varphi$ -direction

$\Delta\Omega$	Solid angle defined by $\Delta\theta$ and $\Delta\varphi$
$\theta_m$	Theta angle into the $m^{\text{th}}$ discretization
$\varphi_n$	Theta angle into the $n^{\text{th}}$ discretization

Abstract of Thesis Presented to the Graduate School  
of the University of Florida in Partial Fulfillment of the  
Requirements for the Degree of Master of Science

CHARACTERIZATION OF THE UNIVERSITY OF FLORIDA SOLAR SIMULATOR AND  
AN INVERSE SOLUTION FOR IDENTIFYING INTENSITY DISTRIBUTIONS FROM  
MULTIPLE FLUX MAPS IN CONCENTRATING SOLAR APPLICATIONS

By

Benjamin Martin Erickson

May 2012

Chair: Jörg Petrasch  
Cochair: David Hahn  
Major: Mechanical Engineering

A high flux solar simulator has been designed, built and put into operation on the campus of the University of Florida. The simulator is capable of reaching measured flux levels of  $4230 \text{ kW/m}^2$  which corresponds to black body stagnation temperatures of approximately 2942 K. The simulator has been installed with several vital subsystems. These subsystems include an XY table, flux measurement setup and data acquisition system. All of the subsystems have been designed with flexibility in mind to allow for a broad range of experiments to be performed by the simulator.

Radiative flux measurements at the focal plane of solar concentrators are typically performed using digital cameras in conjunction with Lambertian targets. To accurately predict flux distributions on arbitrary receiver geometries directional information about the radiation is required. Currently, the directional characteristics of solar concentrating systems are predicted via ray tracing simulations. However, no direct experimental technique to determine intensities of concentrating solar systems is currently available. In this thesis, multiple parallel flux measurements at varying distances from the focal

plane together with a linear inverse method and Tikhonov regularization are used to identify the directional and spatial intensity distribution at the solution plane.

The directional binning feature of an in-house Monte Carlo ray tracing program is used to provide a reference solution. The method has been successfully applied to two dimensional concentrators, namely parabolic troughs and elliptical troughs using forward Monte Carlo ray tracing simulations that provide the flux maps as well as consistent, associated intensity distribution for validation. In the two dimensional case, intensity distribution obtained from the inverse method approaches the Monte Carlo forward solution. In contrast, the method has not been successful for three dimensional and circular symmetric concentrator geometries.

## CHAPTER 1 INTRODUCTION

### **Motivation**

Solar energy research has been on the rise recently. With the increasing costs of non-renewable energy, the search for a cost effective renewable option has been in full swing. One of the largest problems with solar energy is the transient nature of its availability. This is not just limited to the obvious (day and night) but energy levels also fluctuate with passing clouds, atmospheric clarity and the seasons. For concentrating systems, the diffuse to beam fraction of the incoming radiation is important. This fraction is dependent on atmospheric clarity and can be calculated [1]. However, to have the most accurate estimation of energy input this calculation must be performed throughout the experiment and becomes tedious to keep track of. As with any experiment, it is best to perform concentrating solar research in a highly customizable and controllable environment. It is easier to identify important system parameters when all control variables can be easily monitored and adjusted. For this, and some other reasons, a solar simulator is desired. A set of seven elliptical mirrors coupled with Xe-arc lamps are focused to a coincident spot to allow for high flux research. The lamps closely match the spectrum of the sun and thus are good for solar research [2].

An important step in the experimental process is reactor design. Reactors for high heat flux applications must be able to stand up to intense temperatures. Often, concentrating systems are not perfectly focused and have a larger than expected focal spot. This can lead to spillage onto unintended portions of the reactor, causing efficiency losses and potentially catastrophic failures. Additionally, even if spillage is not present, the intensity distribution may be overly concentrated in certain areas leading to

hotspots within the reactor cavity. These hot spots may reach temperatures exceeding the design limit for the materials. With flux mapping systems, the directional character of the incoming radiation is lost. To solve this problem, an inverse method to identify intensity distributions at the focal plane using multiple flux maps is developed. Having the ability to calculate the intensity distribution specific to each concentrating setup allows the experimentalists to successfully design reactors to handle non-uniformities.

### **Literature Review**

Solar energy can be utilized in a plethora of ways. Since this form of power generation is relatively in its infancy, many new and innovative designs are still being presented. No other resource is so abundantly available [3]. Unfortunately, it is extremely transient by nature due to weather, wind and the day and night cycle. All of these shortcomings must be overcome for solar to become a serious competitor in the market. For this reason, it is important to perform lifetime cycle analyses to assess the comparable viability between different solar power generation processes. Attempts have been made in the past by Liu and Jordan [4] and Duffie and Beckman [5].

Parabolic troughs are the most widely used two dimensional trough geometry because it is the most proven and cost effective technology [6]. As of 2002, there were nine commercial scale power plants operating in the Mojave Desert, ranging in size from 14 to 80 MW [6]. As parabolic troughs became more popular, specialized research into all aspects of the design was increased. Thomas and Guven [7] published a review detailing design aspects of such facilities focusing on the structural, optical and thermal subsystems. Parabolic trough technology began to evolve to include secondary reflectors in an effort to decrease losses [8].

A parallel vein of solar research includes the use of three dimensional concentrating optics to obtain higher flux levels. Often, researchers sought to run a Stirling engine by mounting it at the focal point of a sun-tracking dish receiver [9]. Kongtragool and Wongwises [10] compiled a detailed review of the current concentrating solar Stirling engine technology in 2002. Kaushika [11] provides a helpful analysis of the design trade-offs faced by dish collector designers. This report takes into account system cost, reliability and other various system parameters. Large scale central receiver concentrating power plants use a design strategy similar to that of a three dimensional dish. In plants such as Solar One in Barstow, CA and CESA-I in Almeria, Spain [12] the receiver is placed at the top of a tower and a field of heliostats tracks and focuses the sun on the receiver. Very high temperatures are obtainable and the heat is typically stored in a molten salt mixture for later use in steam generation. Other hybrid techniques have been developed and implemented in plants like SOLGAS and CONSOLAR [13].

The transient nature of the availability of solar energy can cause problems in a research environment. For this reason, solar simulators are an attractive option to researchers. Solar simulator systems are typically built using concentrating optics coupled to a Xe-arc lamp. Hirsch et al. [2] are capable of delivering 75 kW of power with peak fluxes of  $4250 \text{ kW/m}^2$  at ETH-Zurich. Similarly, Petrasch et al. [14] designed and built a system that can deliver 50 kW with peak radiative fluxes reaching 11,000 suns. These systems provide a closely controllable environment for solar research and the lamps produce a radiative spectrum similar to that of the sun [15].

In the course of designing an experiment, it can be helpful to have an accurate model to base decisions on. Often in the field of radiation heat transfer Monte Carlo ray tracing is implemented to provide this model. Different Monte Carlo software packages such as Raytran [16] and SHADOW [17] have been developed to address a wide range of needs. However, the Monte Carlo method is not limited to the field of radiation heat transfer. It can be implemented to solve problems in areas ranging from random walk problems [18] to charge transport [19].

A detailed literature survey of inverse problems and flux mapping is presented in Chapter 5.

### **Outline**

This thesis will detail the design, construction and operation of the solar simulator on the campus of the University of Florida. Each subsystem will be detailed in an effort to inform future users of the basic operation of the simulator. Additionally, all of the auxiliary systems such as flux mapping and the XY table are fully specified. These systems are the backbone of the solar simulator and successful operation would not be possible without them. A brief introduction to the Monte Carlo ray tracing program Vegas is given. This program is used to model the simulator and also produce the input files required to test the inverse method. Lastly, the inverse method is presented in full.

## CHAPTER 2 SOLAR SIMULATOR

### **Design**

The design of the solar simulator on the campus of the University of Florida was completed mainly by Professor Jörg Petrasch and Phillip Hauter. Dr. Petrasch and Mr. Hauter used their experience from designing and building previous simulators as the basis for the UF simulator. The simulator design can be broken down into three main aspects; the frame and cooling system, the power system, and the mirror and lamp assemblies. Each of the portions of the design are discussed below.

#### **Frame/Cooling**

The frame of the simulator is the basis for the entire system. It must be sturdy enough to hold of the components and rigid enough to resist the vibrational effects of the fans. The frame for the UF solar simulator (shown in Figure 2-1) uses 90x90 mm Bosch extruded aluminum profile. This material choice allows for a high degree of flexibility in construction while still allowing for the rigidity constraint to be met. Four custom connectors were manufactured to achieve the proper angle for the outside legs.

In addition to the lamp and mirror assemblies, the frame also has to support the cooling system. The cooling system is designed to keep the lamps within the operable temperature in order to reduce the possibility of a lamp shattering. Each mirror and lamp assembly has a dedicated fan attached at the rear of the mirror to achieve the 7.0 meters per second flow rate required for safe lamps operation. These fans run continuously during simulator operation and run for approximately seven minutes after to continue cooling the lamps. In addition, ducts are run to the front of each mirror. Four fans supply air to these ducts that also cools the mirrors and lamps. Figure 2-2

shows the rear view of the simulator. The small fans are attached to the back of each mirror assembly while the larger fans that supply air to the ducts are attached directly to the frame.

## **Power System**

The power system is an important element of the simulator design. Since the power system was first developed for a European electrical grid, a slight redesign was necessary. The 3 phase high voltage supply in Europe runs at 400 Volts as compared to the 480 Volt 3 phase readily supplied in the United States. To accommodate, a power transformer was added to the system, stepping the voltage down to 400 Volts 3 phase. The inside of one of the transformers is shown in Figure 2-3.

All of the power for each lamp runs through the main power box shown in Figure 2-4. Each lamp has its own switch, allowing for individual control of the supplied power to the lamps. The power box is located in the experimental room, behind the simulator so all modifications must be made before running an experiment.

From the power box, the cables run under a cable bridge and to the power rack, shown in Figure 2-5. It is very important to store all of the power equipment in an organized fashion in close proximity to the lamps. This reduces the chance for power loss through the cables and potential interference from outside sources. The power enters the transformers (one for each lamp) and is stepped down to 400 Volt 3 phase. The power then enters a converter (the gray boxes shown in Figure 2-5) and is converted to DC which is then sent to the lamps.

The lamp ignition units, shown in Figure 2-6, are located in close proximity to their corresponding lamp/mirror assembly. Lamp ignition is a very delicate process. Initially the lamp requires high voltage (approximately 40 kV) and low current but when the arc

is generated the power supply must quickly change to lower voltage and high current (approximately 150 Amps). Currently, the lamps are controlled by a LabView program. Each lamp can be individually turned on or off and the power level can be adjusted. Additionally, the reading from the flux sensor has been integrated to the front panel so only one LabView program must be running during an experiment. A screen shot of the program is shown in Figure 2-7.

### **Mirrors/Lamps**

The last portion of the simulator design is the lamp and mirror assembly. Important parameters of the mirrors and lamps are listed in Tables 2-1 and 2-2. The assembly must hold the mirror and lamp securely while still allowing for coarse and fine adjustment of the focal spot. Using a detailed set of schematic drawings, the basic mirror assemblies (Figure 2-8) are positioned on the frame. Each mirror is an identical 3D ellipse and all are aligned to have one coincident focal point (Figure 2-9). The lamp for each assembly sits at the other focal point of the mirror. This allows all light emitted from the lamp to be concentrated onto the coincident focal point. The mirror is locked into position on the holder assembly. The lamp is inserted carefully from the front, through the opening in the rear of the mirror. A metal rod on the front of the mirror provides support on to the lamp to prevent breakage. The rod is specially designed to allow expansion during operation without putting stress on the lamp. An ignition box is mounted directly to the frame below the each lamp. The completed mirror and lamp assembly is shown in Figure 2-10.

### **Installation**

After unpacking and organizing all of the parts, the frame was the first thing to be constructed. Using a detailed set of drawings (Appendix A) the frame was completed

and secured to the floor using concrete anchor bolts. Next, the mirror holder assemblies were attached in their appropriate positions on the frame. The frame for the protective shutter was then installed in between the simulator frame and the focal plane. Figure 2-11 shows the finalization of the position of the simulator frame. The laser level seen in the forefront of the picture was used in conjunction with a mounted measuring stick to accurately place the frame cross supports.

The next step after the frame and mirror holder assemblies were properly aligned was to add the mirrors and lamps. After they were secured, the mirror holder assembly positions were again adjusted to be as close as possible to the drawings. With everything in place, the ignition box for each lamp was installed and the wiring from the power rack was completed. The ignition units are placed as close to the lamps as possible to prevent transmission losses. Each grouping of cables includes a ferrite ring to reduce noise interference. This was necessary because of problems with the image capture system. Since the camera is so close to the simulator, the picture would be distorted during startup and shutdown. This was mitigated with the addition of the ferrite rings. The cooling system was the last element to be installed. The fans were mounted to the frame and ducts were run to the front of each mirror. Figure 2-12 shows the installation of the power and cooling systems on the rear of the simulator.

### **Focusing**

Focusing is of the utmost importance. Since the simulator consists of seven individual elliptical mirrors, the focusing process must be carried out for each of them. The only way to accurately focus the mirrors is to manipulate them while the simulator is in operation. It is important to take all safety precautions outlined in Appendix B. It should be noted that only Professor Petrasch was allowed to enter the experimental

area while the simulator was on. Each lamp was turned on individually and, through use of the flux mapping system, was focused. The mirror holding assemblies are uniquely manufactured to allow as much adjustment as possible. Each assembly includes three screws accessible from the rear to accurately locate the lamp. Additionally, the entire mirror assembly was shifted on the frame when the fine adjustment via the mirror holder assembly was not adequate. After all seven assemblies were individually focused all were turned on to verify a unified focal spot.

### **Safety**

The simulator is an extremely dangerous device. For this reason, many safety protocols have been put in place. Extensive startup and shutdown procedures and general safety warnings have been compiled in Appendix B. Along with these procedures, many safety systems have been implemented for the protection of the users of the simulator. Many experiments involve high temperatures and pressures. Complicating the potential for the simulator bulbs to shatter, there is a high risk of debris flying through the experimental area. To address this, Plexiglass sheets have been installed over the windows, protecting the control room. Figure 2-13 shows the removable window protection.

Another concern is the possibility of someone entering the experimental area unannounced while the simulator is in operation. To eliminate the possibility of this happening, all of the doors are interlocked. Figure 2-14 shows an example of a door safety interlock and Figure 2-15 is a schematic floor plan showing the location of each door interlock. All interlocks are wired back to the safety panel in the control room. The safety panel is a centralized box that allows the user to easily assess the state of the experimental area without entering it. Each interlock has a corresponding light which is

illuminated when the interlock is active (closed). In addition to the doors, the individual fans on the mirror holder assemblies are interlocked and controlled at the safety panel. A simple switch turns them on and then seven lights illuminate to show all the fans are operational. Additionally, the fans run for seven minutes after shutoff to continue cooling the lamps. The shutter in front of the simulator is also controlled at the panel via a switch and push button. Once all of the interlocks are engaged power can be supplied to the simulator by throwing one final red switch. The safety panel is shown in Figure 2-16. All switches are clearly labeled on the panel. If any interlock is tripped during operation power is immediately cut from the system and the shutter will return to the down position.

### **Peripheral Subsystems**

Peripheral subsystems are necessary for successful completion of any experiment. They provide flexibility and allow for a wide range of experiment types to be performed using the simulator. The main subsystems for the simulator are the XY table, flux target, MATLAB, camera and data acquisition systems.

#### **XY Table**

It is crucial for a solar simulator to have a way to remotely move experiments in and out of the focal spot. For example, most experiments require the measurement of the flux via a Lambertian flux target. This is typically mounted to the side of the experimental reactor and the mounting apparatus is moved to put the flux target and then the reactor into to the focal spot. This is most easily accomplished by using a XY table. To meet this need, the BiSlide dual rail XY table manufactured by Velmex Incorporated was installed. The user manual along with more information about the XY table can be found in Objects 2-1, 2-2 and 2-3. The user manual outlines proper care

and maintenance which includes lubrication. Before applying the lubricant, the slides should be cleaned out using the air compressor. Once a month the supplied lubricant (found in the back of the work area) should be applied to either side of carriage and the slide should be moved from end to end to distribute evenly.

The table has approximately an 80 centimeter range in the planar (parallel to the face of the simulator) direction and a 40 centimeter range in the axial direction. This allows for enough movement to mount a small to medium reactor and flux target by each other and still be able to move each to the focal spot. The dual rail system was chosen to increase stability for loadings with eccentricity. A simple mounting plate was installed with multiple holes for easy configuration to meet the needs of support systems for any experiments. The XY table assembly is shown in Figure 2-17. The table has a resolution of 0.005 millimeters to allow for extremely precise positioning. It has a repeatability of 0.005 millimeters over the short term and 0.010 millimeters after sustained usage when using the homing function.

The table also came with a program to allow movement to be controlled remotely. The program, "COSMOS," allows for individual input or for pre-programmed movements. Simple text files can be run in COSMOS, making it easy to relocate the reactor. For example, a program was written to zero the XY table and move it back to center the flux target in the focal spot. To increment the table, first ensure the control module is turned on (in the experimental area). Next, open the VXM software "COSMOS." Change the entry mode in the terminal from immediate to buffered and then type the desired command into the command line. Basic commands are posted by the computer and more advanced commands can be found in the VXM user manual. Object 2-4 contains

the user manual for the XY table control system (VXM). This is very convenient and simplifies the experimental process. Figure 2-18 shows a screen shot of the COSMOS software terminal. Simple movements are outlined in the XY table document (found in Appendix C) which is also posted in the control room.

### **Flux target**

The flux target is a vital subsystem for the solar simulator. It allows for a complete flux map to be measured before or after the experiment is run. The target was manufactured out of two solid pieces of aluminum. The main piece was milled to have channels to allow for cooling water to be circulated in order to evacuate the heat absorbed by the target (Figure 2-19A). This piece also has a groove for a gasket and many tapped holes to allow the back plate to be attached securely. The gasket provides a seal to eliminate leakage. The back plate is a thin piece of aluminum drilled through to allow attachment to the main portion. A drawing of the flux target is available in Appendix C.

The front of the flux target was designed to be Lambertian or diffuse in nature, reflecting incident radiation evenly in all directions (Figure 2-19B). To accomplish this, a thin coating of aluminum oxide spray paint is applied to the front surface of the target. In one of the targets a through hole was drilled and tapped to accommodate a heat flux gauge from Vatel Corporation. This heat flux sensor measures the flux and allows for calibration of the flux mapping system (see Chapter 3 for more detail). A second flux target was manufactured without the hole for the heat flux sensor so unblemished flux maps can be taken in the future.

## Camera and MATLAB

The other portion of the flux measurement subsystem is the camera. An industrial grade CCD camera from Basler (model #: scA1300-32gm) was purchased in addition to a 35 mm focal length focusable double gauss lens from Edmund Optics. Object 2-5 links to the user manual for the camera and more information is available in Objects 2-6 and 2-7. Detailed information about the camera is available in Table 2-3. The camera is mounted within the solar simulator and pointed at the focal spot. The extremely high intensity levels generated by the simulator make it necessary to have a lot of filtering in front of the camera to protect it. The setup uses neutral density absorptive filters ranging in optical density from 1.0 to 5.0. These optical densities correspond to transmission values of 10% and 0.001%, respectively. To handle the variable flux levels the simulator can generate (i.e. turning on three lamps instead of seven) a filter wheel with these varying levels of filter has been mounted in front of the camera. Before the experiment takes place the wheel is moved to the appropriate filter to protect the camera and give the best image. The camera and filter wheel setup is shown in Figure 2-20.

The camera is connected to a computer in the control room via a gigabit Ethernet cable. A MATLAB program has been developed to create a real time visualization of the picture from the camera. Before an experiment starts it is important to initialize the flux mapping software to ensure the reactor is in the correct location. By removing the filtering from the camera it is easy to identify if the reactor is properly placed. Once confirmed, the filter must be replaced and the experimentalist can continue through the startup checklist. The program includes options such as “deskew” (to account for the off axis picture), “adjust” to scale the output and the option to show in black and white or

another color scheme. It also includes the ability to save pictures for later analysis. This functionality is used to generate flux maps. A full listing of the capabilities and inputs for the MATLAB program is available in Appendix C and the source code is given in Objects 2-8 and 2-9.

### **Data Measurement (DAQ)**

Every experiment will require measurement of different variables, some more complex than others. Currently, a data acquisition unit (DAQ) from National Instruments is installed in the solar simulator room. The DAQ has five modules installed with two empty spaces for extra modules; NI 9203 analog current input, NI 9264 analog output, NI 9213 thermocouple input, NI 9485 relay, NI 9205 analog input. More details about the individual modules are listed in Table 2-4. This setup provides flexibility and can meet the needs of many different experimental setups. The DAQ is mounted inside a protective case which also houses the control module for the XY table. This box, shown in Figure 2-21, is in the experimental area and is hardwired into the control room as well.

[Object 2-1. The XY table user manual \(.pdf 251 KB\)](#)

[Object 2-2. The XY table extended user manual \(.pdf 1.166 MB\)](#)

[Object 2-3. Extra information pertaining to the XY table \(.pdf 2.116 MB\)](#)

[Object 2-4. XY table control \(VXM\) user manual \(.pdf 789 KB\)](#)

[Object 2-5. CCD camera user's manual \(.pdf 2.244 MB\)](#)

[Object 2-6. General information about the CCD camera \(.pdf 1.249 MB\)](#)

[Object 2-7. Supplementary information about the CCD camera \(.pdf 382 KB\)](#)

[Object 2-8. Source code for the flux mapping software \(.txt 6 KB\)](#)

[Object 2-9. Function findminmax necessary to run flux.m \(.txt 1 KB\)](#)

Table 2-1. Parameters of the simulator mirrors.

Parameter	Value
Semi-major axis, a (m)	1.0201
Semi-minor axis, b (m)	0.4802
Depth (m)	0.4557
Estimated mirror error (mrad)	5.0
Estimated mirror reflectivity (-)	0.92

Table 2-2. Parameters of the simulator lamps.

Parameter	Value
Power (kW)	6.0
Required air speed for cooling (m/sec)	7.0
Operating voltage (V)	35
Maximum operating current (A)	170
Ignition voltage (kV)	40

Table 2-3. Parameters of the camera and lens.

Parameter	Value
Focal length (mm)	6.0
Sensor size (in)	1/3
Maximum frame rate (fps)	32
Number of pixels, vertical (-)	960
Number of pixels, horizontal (-)	1280

Table 2-4. Parameters of the DAQ modules.

Module	Channels	Resolution (bits)
NI 9203	8	16
NI 9264	16	16
NI 9213	16	24
NI 9485	8	-
NI 9205	32	16



Figure 2-1. The frame of the simulator at the beginning of construction. Photo courtesy of Ben Erickson.



Figure 2-2. The simulator from behind. Photo courtesy of Ben Erickson.

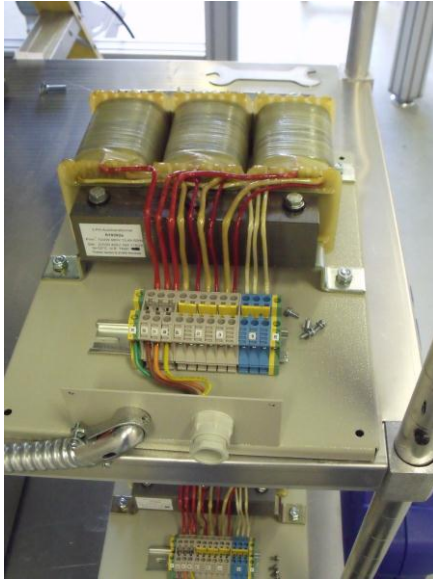


Figure 2-3. The inside of one of the power transformers. Photo courtesy of Ben Erickson.



Figure 2-4. Power to each lamp can be individually turned on or off at the main power box. Photo courtesy of Ben Erickson.



Figure 2-5. The power rack houses a converter and transformer for each lamp assembly on the simulator. Photo courtesy of Ben Erickson.



Figure 2-6. Ignition unit mounted below its corresponding mirror/lamp assembly. Photo courtesy of Ben Erickson.

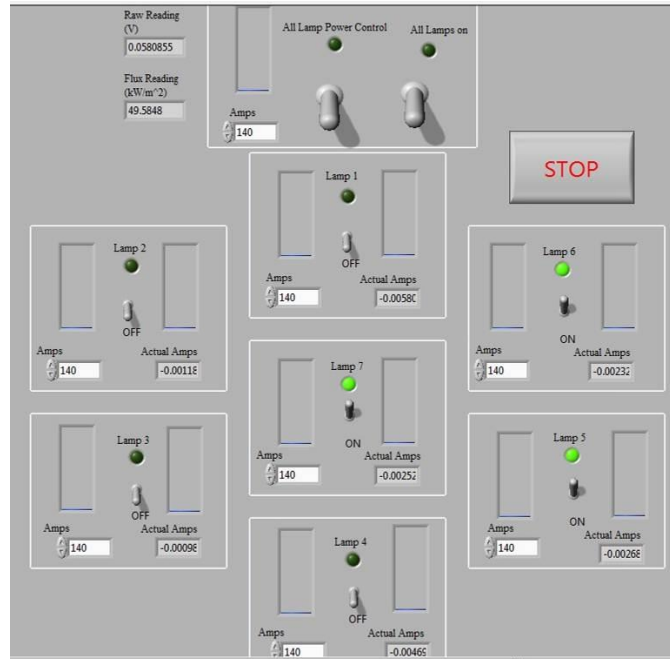


Figure 2-7. LabView program designed to control the lamps and read the flux sensor.



Figure 2-8. Each mirror has a holder assembly (shown above) which allows for coarse and fine adjustment of the focal point. Photo courtesy of Ben Erickson.

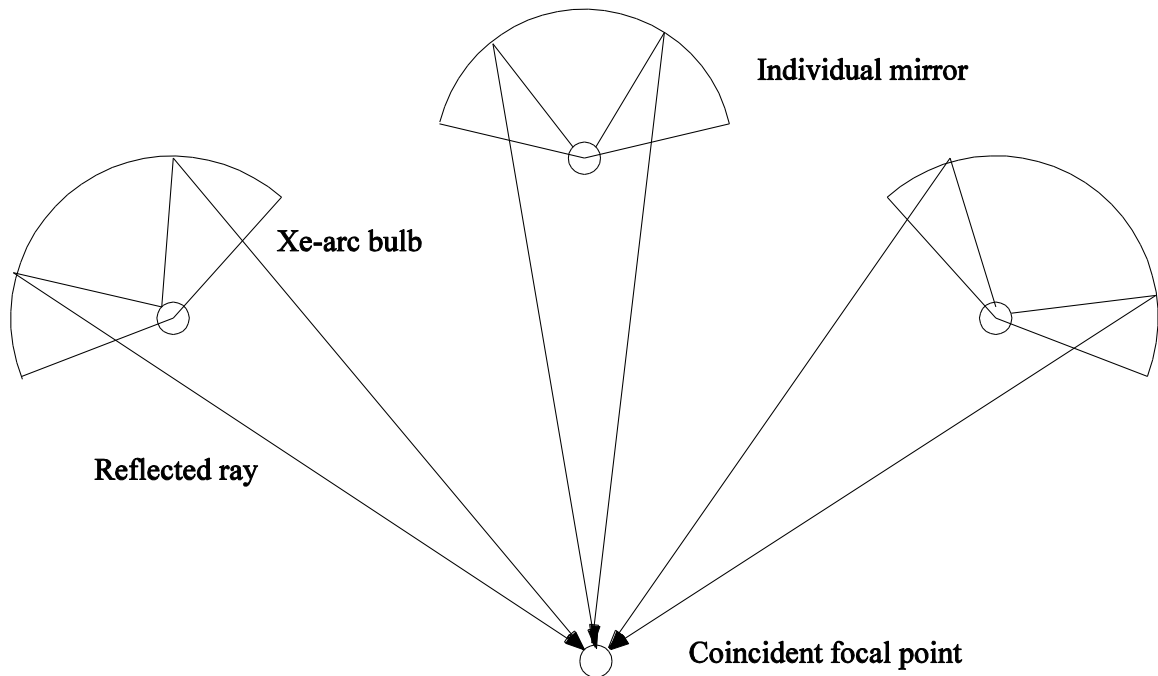


Figure 2-9. Schematic drawing showing a set of elliptical lamps with a single coincident focal point.

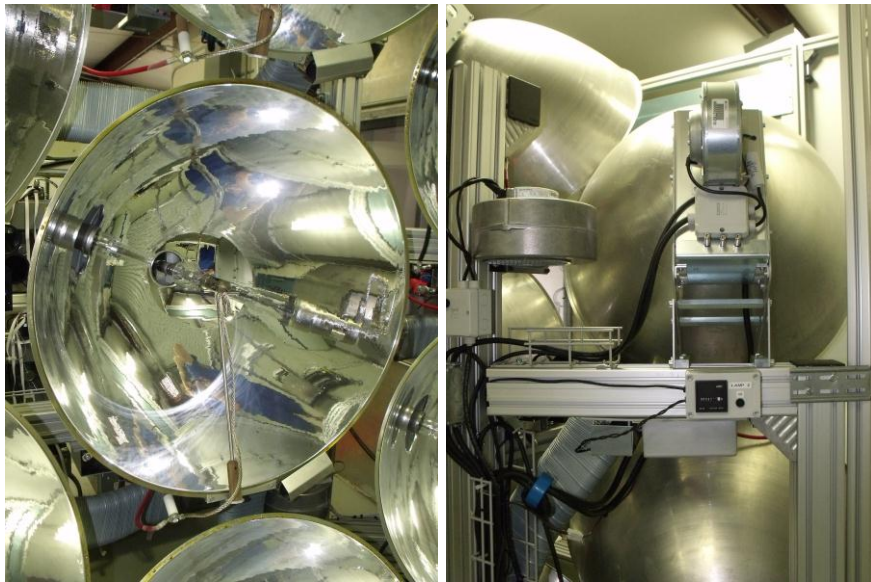


Figure 2-10. A completed mirror and lamp assembly shown from the front and back. Photos courtesy of Ben Erickson.



Figure 2-11. Phillip Hauter working to assemble the simulator frame. Photo courtesy of Ben Erickson.



Figure 2-12. Installation of the power and cooling systems. Photo courtesy of Ben Erickson.



Figure 2-13. The windows into the control room are protected by removable plexiglass sheets. Photo courtesy of Ben Erickson.



Figure 2-14. Two safety interlocks protecting the rear doors during operation of the simulator. Photos courtesy of Ben Erickson.

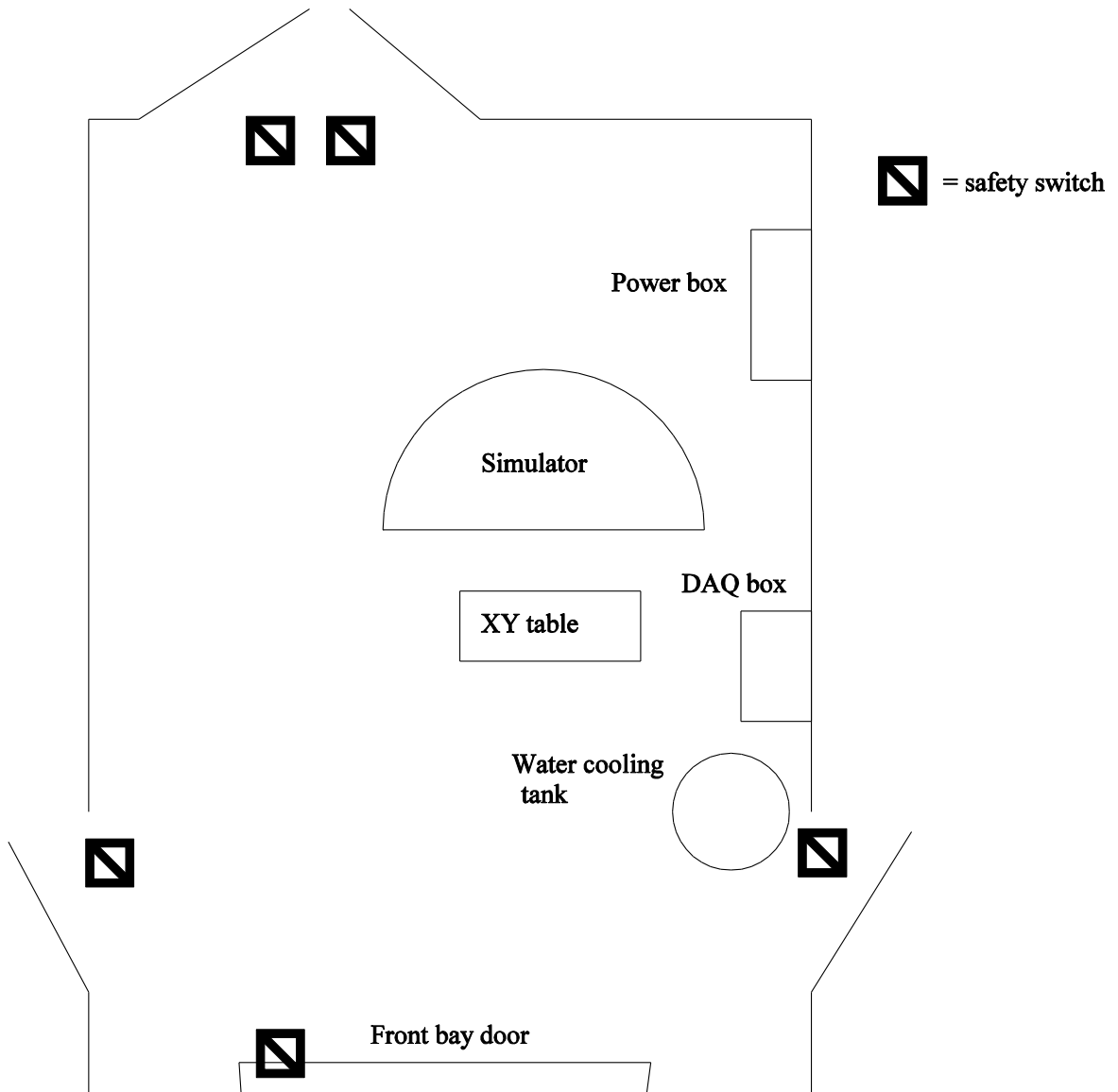


Figure 2-15. Schematic floor plan of the experimental area showing the location of the safety interlocks. Every door is interlocked to ensure safe operation.



Figure 2-16. The safety panel which alerts the users to open doors and allows for power to be supplied to the simulator if all interlocks are active. Photos courtesy of Ben Erickson.

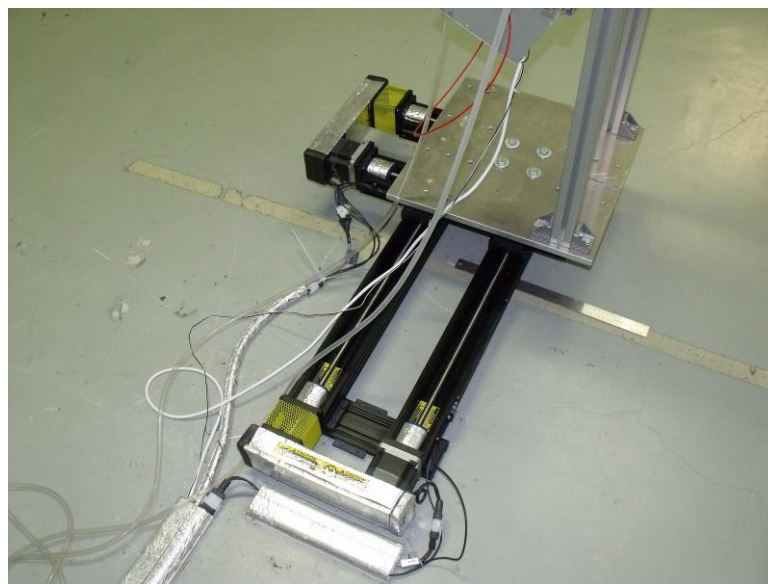


Figure 2-17. The Velmex BiSlide XY table. Photo courtesy of Ben Erickson.

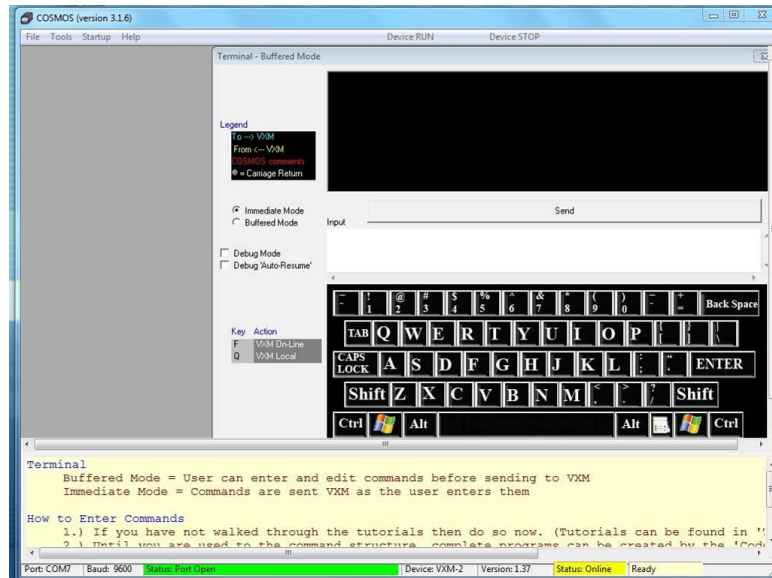


Figure 2-18. Screen shot of the XY table control program “COSMOS.”

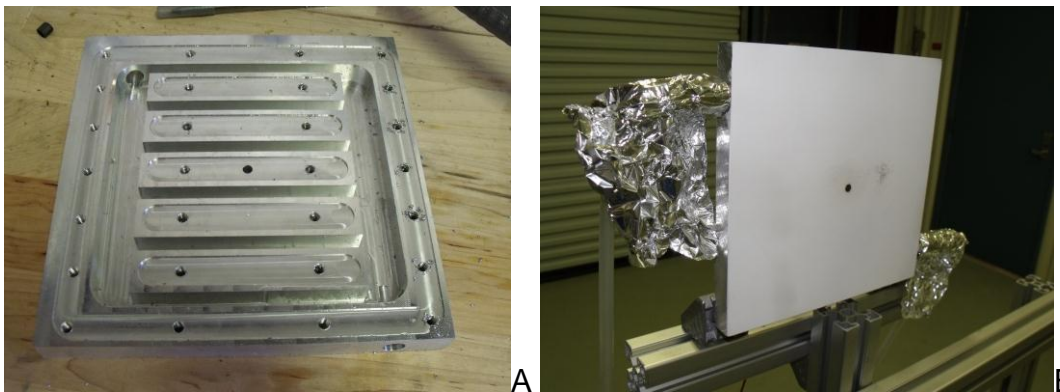


Figure 2-19. The flux target shown open from the back (left) and painted and setup (right). Photos courtesy of Ben Erickson.



Figure 2-20. The CCD camera and filter wheel. Photo courtesy of Ben Erickson.

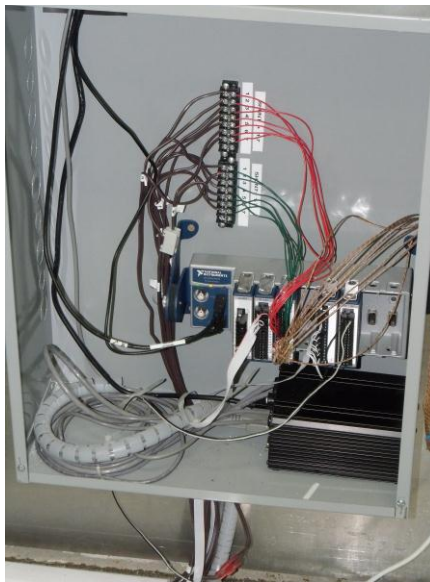


Figure 2-21. The DAQ and protection box in the simulator room. Photo courtesy of Ben Erickson.

## CHAPTER 3 MONTE CARLO SIMULATION

The purpose of the solar simulator is to provide an easily controllable experimental facility for research into solar processes. Monte Carlo ray tracing simulations are often employed to predict the behavior of such systems. Monte Carlo simulations allow the experimentalist to obtain prior information about how the system will respond while allowing the model to be easily modified. They work based on a statistical sampling technique known as the Monte Carlo method [20]. In general, every variable included in the simulation is defined by an individual probability distribution function. Using the PDF, a cumulative distribution function is created and then inverted. Generating a random number to be substituted into the inverted cumulative distribution function produces a value for the desired variable. This value is randomized in the same manner for subsequent runs and after enough runs, an accurate estimate of the outcome (flux or intensity distribution) can be made. For example, a ray is traced to a surface. Knowing the surface properties, we generate a random number that tells us if the ray is absorbed, reflected or transmitted. The ray is traced until extinction and its ending location is recorded. This method can be used to generate flux maps that closely match the real maps produced by the simulator. More detailed reading on the Monte Carlo method can be done in books by Modest [20], Hamersley and Handscomb [21], Cashewell and Everett [18] and Schreider [22].

### **Monte Carlo Simulations**

An in-house Monte Carlo ray tracing program [23] was used to model 2D and 3D concentrating systems. The program has a library of geometries that can be customized to model most concentrating systems. It also features angular binning, which allows for

the output of the intensity distribution at any desired location. The Vegas model provides the intensity distribution as well as the consistent, associated flux distribution, allowing for in-depth validation of the inverse method.

### **Simple Simulations**

Vegas has a large library of predefined geometries that can be implemented to model most concentrating systems. The FORTRAN code is free and open source and available by contacting Professor Petrasch ([joerg.petrasch@fhv.at](mailto:joerg.petrasch@fhv.at)). It contains reflection options ranging from fully diffuse to a mix of partially transparent with specular reflection. A complete list of the general input parameters for reflector geometries is contained in the manual (Object 3-1). When starting with Vegas it is best to begin with simple setups. Table 3-1 and Figure 3-1A show the setup and Vegas output for a simple disk, respectively. Figure 3-1B shows a slightly more complicated geometry, an elliptical dish. Using a compilation of simple geometries, the user can build and customize whatever model they require.

### **Simulator Model**

The simulator at UF was successfully modeled in Vegas and is shown in Figure 3-2. The model consists of seven elliptical mirrors coupled with circular sources at one focal point. The other focal point of each mirror is aligned to coincide at the focal plane. The resulting flux distribution is shown in Figure 3-3. By modifying the size of the circular source to match the estimated size of the Ze-arc and adjusting the reflection error in the mirrors the focal spot size can be adjusted to approach that of the actual simulator. Figure 3-4 shows the flux distributions for varied reflector error. The reflector error of 5 mrad and source size of 7.5 mm was shown to be the best approximation of

the actual simulator. However, the exact shape of the focal spot on the real simulator has an asymmetry that cannot be fully modeled in Vegas.

### 2D Case for Intensity

The Vegas code also affords us much flexibility in optimizing the parameters of input for our inverse code. Rather than run experiments every time a change in parameters is required, we can simply change the input to Vegas and receive experimental data. While this data will lack the errors we eventually wish to compensate for, the output is sufficient to optimize the code. Once the optimal input is found, experimental data from concentrating systems can be easily obtained.

### 3D Flux to Intensity

Vegas can also produce the intensity results for a fully three dimensional case. However, a fully three dimensional intensity distribution causes many problems when attempted to be represented graphically. The distribution cannot be simply displayed via a contour or 3D plot because it has five dimensions (two special, two directional and the value of intensity). This fact, combined with the numerical difficulty of highly ill conditioned matrices (read more about this in Chapter 5) makes the 3D solution not feasible at this time.

[Object 3-1. User's manual for the Monte Carlo ray tracing program Vegas \(.pdf 595 KB\).](#)

Table 3-1. Parameters required to implement a ring in Vegas.

String	Parameter type	Description
X_C=	Real	X-component of center point C
Y_C=	Real	Y-component of center point C
Z_C=	Real	Z-component of center point C
X_N=	Real	X-component of normal vector $n$
Y_N=	Real	Y- component of normal vector $n$
Z_N=	Real	Z-component of normal vector $n$
R_1=	Real	Inner radius of ring
R_2=	Real	Outer radius of ring

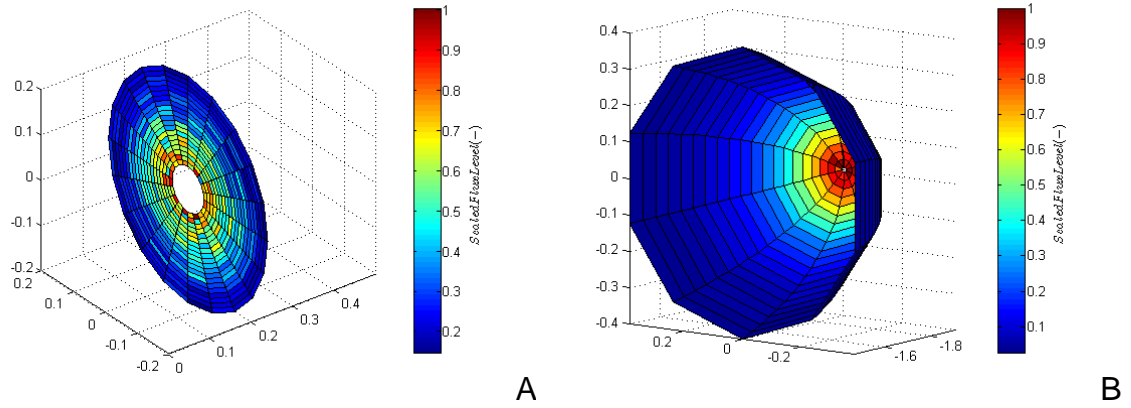


Figure 3-1. A simple disk (A) and elliptical dish (B) modeled in Vegas.

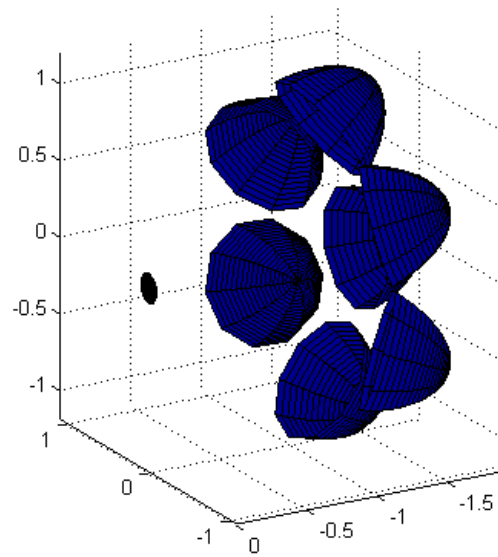


Figure 3-2. The simulator as modeled in Vegas with 5.0 mrad reflection error and 7.5 mm bulb diameter.

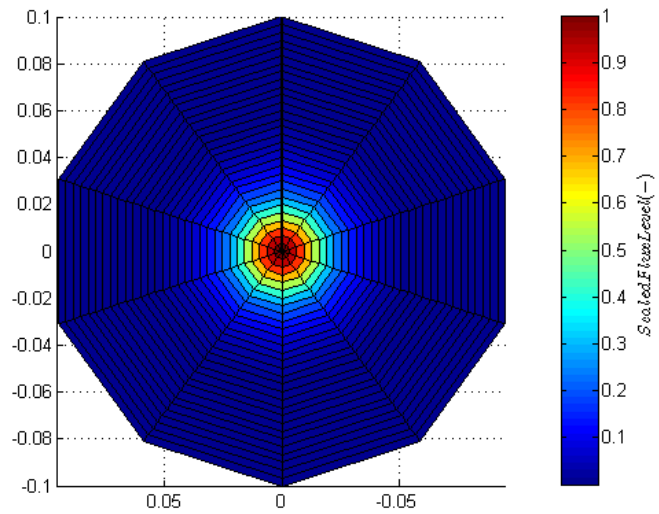


Figure 3-3. Target plot for the simulator modeled with 5.0 mrad reflection error and 7.5 mm bulb diameter.

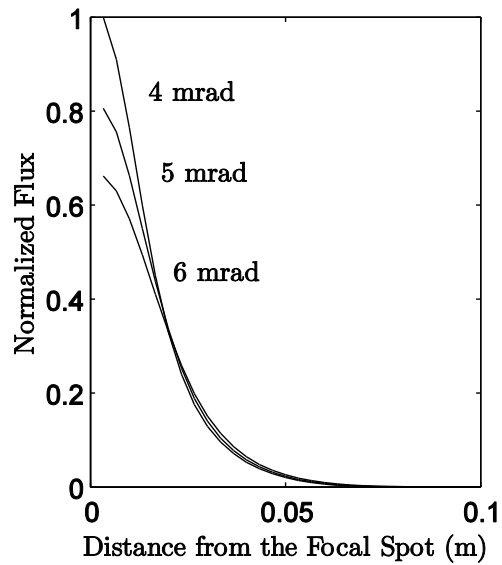


Figure 3-4. Flux distribution at the focal plane for varying reflection errors.

## CHAPTER 4 EXPERIMENTS

A complete flux map is the first step in fully characterizing a concentrating solar facility such as a solar simulator. Without knowing how much power the system can supply, trying to design an experiment is pointless. To optimally design a reactor, the experimentalist must take into account many variables. Included in consideration is maximum temperature along with the characteristics of the incoming beam. Flux maps also provide the basis for efficiency and other calculations by supplying a full map of the radiative energy incident on an experiment. Due to their ability to help identify these parameters, flux maps are essential in assessing the potential success or failure of an experiment.

### **Flux Measurements**

A point flux measurement is easily obtainable through the use of a flux sensor. The solar simulator at UF uses a flux sensor provided by Vatell, Corp. It measures the voltage difference across a thin foil disk to obtain the incident flux measurement. The schematic drawing for the flux gauge is shown in Figure 4-1 and the certification sheet from the most recent flux gauge is available in Appendix C. The flux sensor is threaded to allow for easy insertion from the rear of the flux target. Once fully mounted, the flux target is moved to the desired location and a flux reading can easily be obtained through LabView using the provided calibration data. A schematic of a typical flux measurement setup is shown in Figure 4-2.

### **Flux Mapping**

Once the flux sensor has been successfully setup and integrated into LabView the next step is to create a flux map. Obtaining a flux map at a given plane is easily

achieved using a Lambertian target and a charge-coupled device (CCD) camera in conjunction with a flux sensor to calibrate images [24]. Typically, a water cooled Lambertian target is first positioned at the focal plane. With careful use of filters, a highly linear digital camera is then used to acquire an image of the irradiated target using Matlab. The brightness of each pixel of the digital image is proportional to the radiative flux incident at the target location corresponding to the pixel. A flux measurement device is then used to establish the relation between pixel brightness and energy flux.

An example raw image is shown in Figure 4-3A. The program “flux.m” has been developed to simplify the image capture process. This program allows for a real time video stream from the camera so the experimentalists may view the target or reactor without risking harm to their eyes. It also allows for the capture of images and saves them to a predetermined folder for later analysis. Through post image processing the images can be rendered into color which relates directly to the flux level. Figure 4-3B shows a post-processed flux map. The discoloration (blue spot) at the middle of the focal point shows the position of the flux gauge. By moving the flux target to the left or right and recording another picture and flux measurement a scale correlating pixel value in the image to flux level can be created. By this method, a complete flux map of the focal plane can be generated. The calibration results for the simulator are shown in Figures 4-4 and 4-5. Figure 4-4 shows the calibration curve for four spots along the focal plane. These points show a linear relationship and the slope is used to convert pixel value to flux level. This calibration curve will only be valid for the filtering level predetermined by the experimentalist via the filter wheel. For the flux map shown in

Figure 4-5, only lamp 7 was used with a filter having an optical density of 4.0. For best results, flux maps should be completed before and after every experiment.

Another use for the flux mapping system is reactor observation during experimentation. Due to the high intensity of the radiation it is dangerous to look directly at the focal spot during operation. Welding glasses are available in the control room to allow direct observation but the detail that can be seen with these is limited. However, reactors can be indirectly observed through the flux mapping system. Figure 4-6 shows an image captured during an experiment. The area where spillage around the aperture occurs was monitored for deterioration throughout the experiment. If anything had begun to go wrong the experimentalist can see it first on the flux mapping system and shut down the system to address the issue. It is just one more safety mechanism to ensure the safe operation of the solar simulator.

### **Simulator Flux Maps**

The flux mapping system was used to focus and create a map for each lamp. The results for lamps 5 and 7 are shown in Figure 4-7. Lamp 5 is off center with relation to the flux target whereas lamp 7 is directly on axis. This accounts for the lower flux level and wider flux distribution for lamp 5 as compared to lamp 7. The measured flux (measured at the blue discoloration on the map) for lamp 5 and 7 was 398 and 799  $\text{kW/m}^2$ , respectively. As more lamps are added the flux distribution becomes larger as well as more intense. Figure 4-8 shows the distribution when lamps 2 and 6 are turned on simultaneously, resulting in a measured flux of 1248  $\text{kW/m}^2$ . One danger of improper filtering is image saturation. This is illustrated in Figure 4-9. The camera reaches its maximum pixel value and so all information is lost in the red region. The flux reading for lamps 2, 4, 6 and 7 being on was 2842  $\text{kW/m}^2$ . It should be noted that the

lamps were operating at approximately 75% power when these flux maps were taken (140 A).

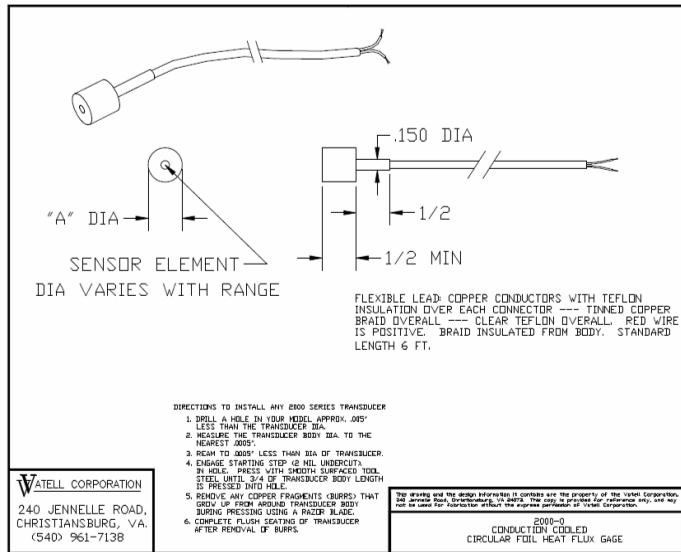


Figure 4-1. The schematic drawing for the flux sensor from Watell, Corp.

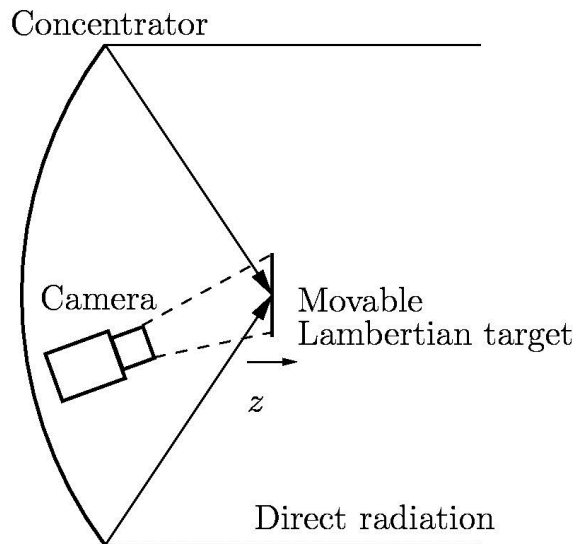


Figure 4-2. A schematic drawing of a typical flux measurement setup.

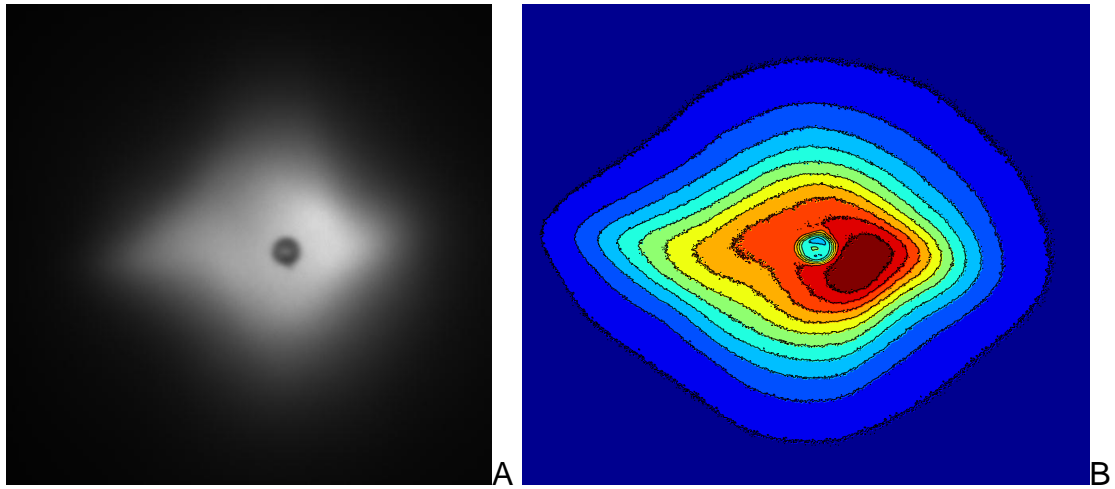


Figure 4-3. A raw (A) and post processed (B) image collected by the flux mapping system before calibration data is applied.

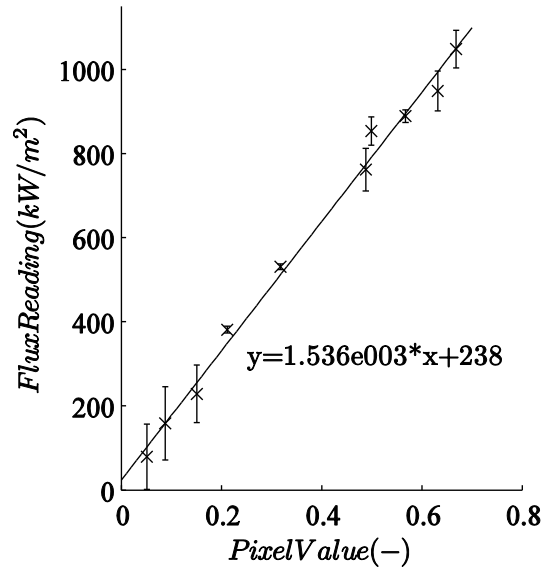


Figure 4-4. Calibration curve relating pixel value to flux level.

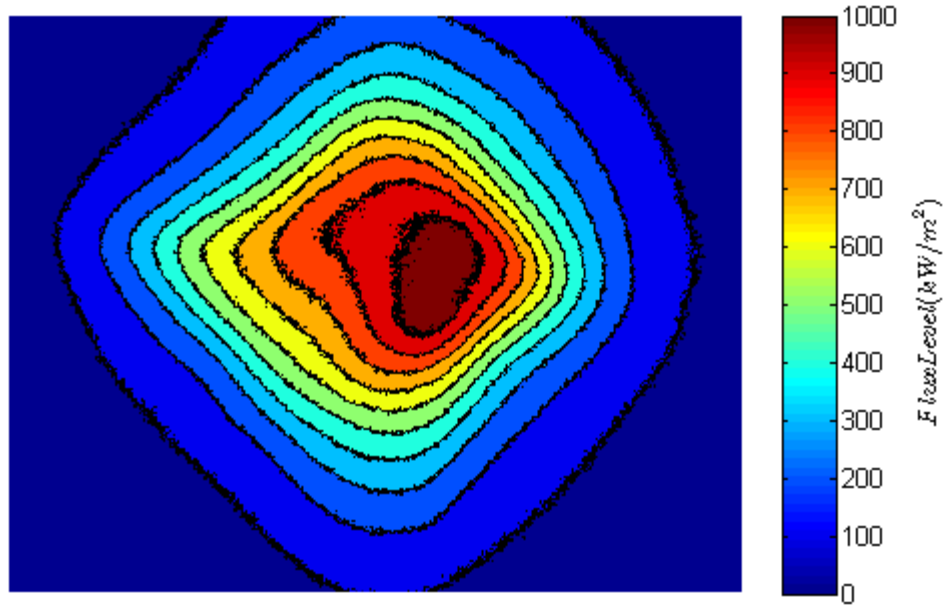


Figure 4-5. A completed flux map of lamp 7 with the sensor discoloration removed.

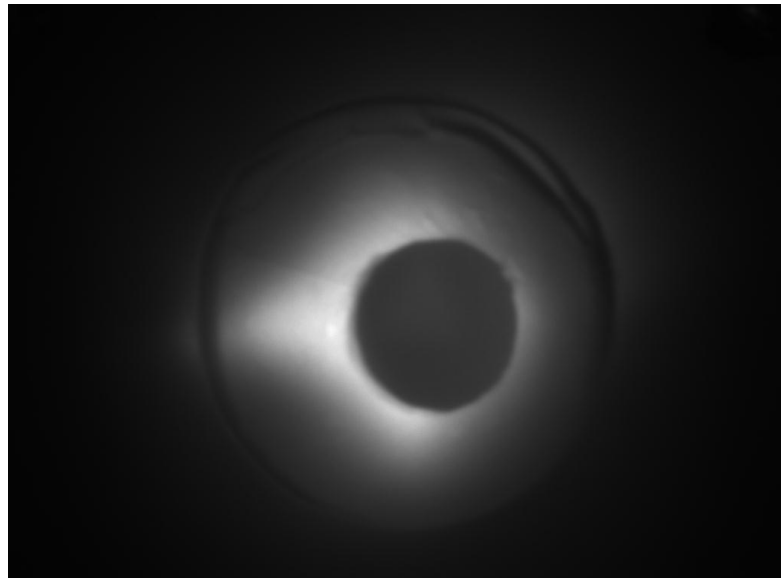


Figure 4-6. A raw image of a reactor during experimentation showing slight spillage onto the aperture.

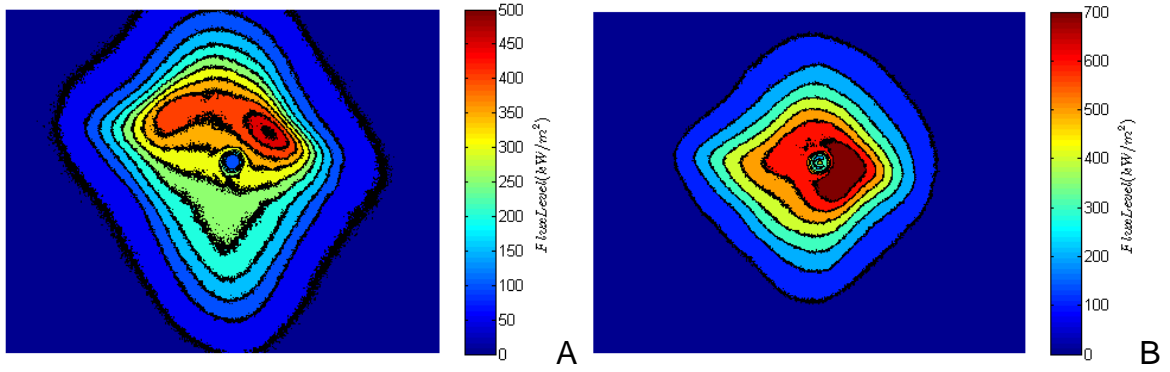


Figure 4-7. Flux map from the simulator with lamp 5 (A) or lamp 7 (B) turned on.

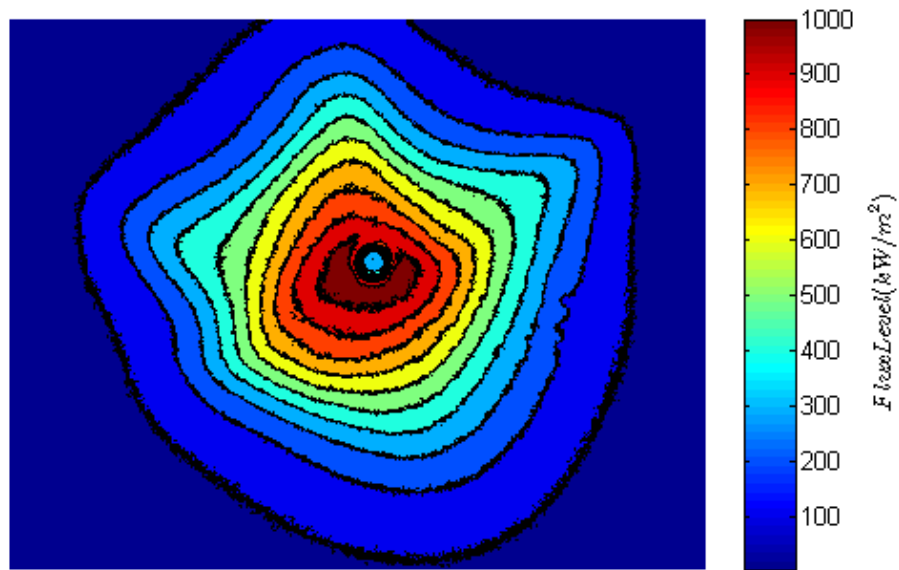


Figure 4-8. Flux map from the simulator with lamps 2 and 6 turned on.

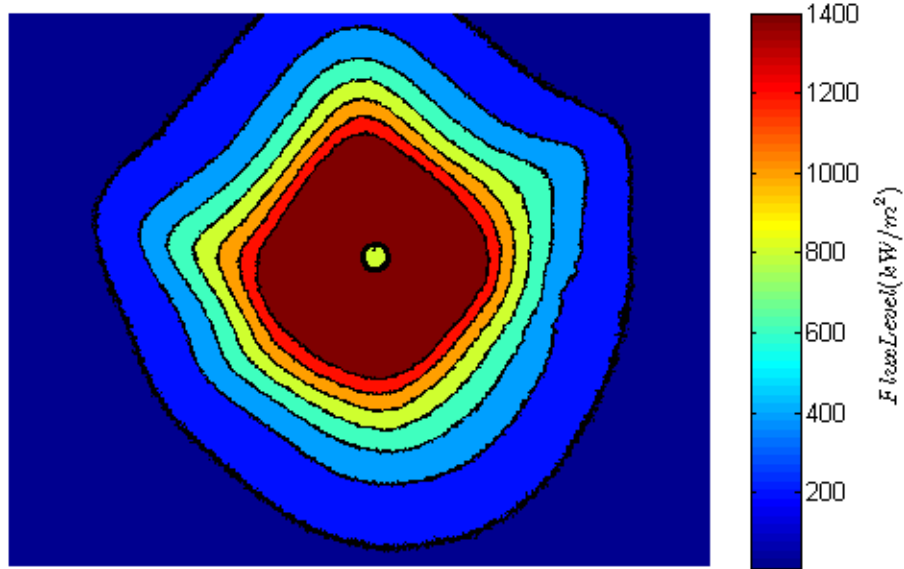


Figure 4-9. Flux map from the simulator with lamps 2, 4, 6 and 7 on illustrating saturation due to not enough filtering.

## CHAPTER 5 INVERSE METHOD<sup>1</sup>

### Introduction

Solar concentrating systems and high flux solar simulators produce high radiative flux levels. Hirsch and Steinfeld [2] have reported fluxes in excess of  $4,250 \text{ kW/m}^2$  for an elliptical trough based solar simulator. Petrasch et al. [14] have reported fluxes as high as  $11,000 \text{ kW/m}^2$  from an array of elliptical reflectors coupled to Xe arc lamps. These flux levels are equivalent to blackbody stagnation temperatures of 2945 and 3730 K, respectively. Linear systems such as the EuroTrough [25] parabolic concentrator achieve actual temperatures of roughly  $500 \text{ }^\circ\text{C}$  with concentration ratios of approximately 82:1. The LS-1 and LS-2 parabolic troughs by Luz International Ltd. [26] have geometric concentration ratios around 23:1, achieving temperatures near  $400 \text{ }^\circ\text{C}$ . Flux mapping systems are essential for any experimental concentrating solar energy system. They provide an accurate measurement of the radiative flux distribution in the focal plane and thus form the basis for energy balances and efficiency calculations [5, 6]. Flux mapping systems consist of a diffusely reflecting flux target in the focal plane of the concentrator, a highly linear charge-coupled device (CCD) camera [5–7, 9] and a flux sensor for calibration [7, 8].

Typically, ray-tracing programs such as CIRCE2 [31], and VEGAS [23] are used to simulate flux and intensity distributions. These systems rely on idealized reflector geometries and they are adequate for the design of concentrating systems. However, they fail to predict non-ideal flux and intensity distributions due to surface imperfections introduced during manufacturing or operation [32].

<sup>1</sup>The majority of the material from this chapter is taken from the conference paper “Inverse identification of intensity distributions from multiple flux maps in concentrating solar applications” submitted and presented at EURO THERM 95 in Nancy, France.

In this paper, an experimentally based, inverse method to determine the intensity distribution at a desired solution plane is presented. The method uses multiple flux maps at varying distances along the concentrator's axis as an input to solve for the intensity distribution at the solution plane. There are two main approaches to solving inverse radiation problems, (i) iterative and (ii) direct methods. The iterative approach is based on an assumed parametric model of the intensity function. An optimal solution of then intensity is then found by minimizing the associated residual functionals [33]. While iterative methods are often more stable than direct methods, they are typically nonlinear and suffer from larger computation time [33]. Direct methods are based on discretizing the physical relations between measured (flux) and unknown (intensity) quantities and solving the resulting system of equations. Direct methods often result in ill conditioned linear systems of equations. A range of inverse problems involving radiation in participating medium have been studied in [34–39]. In the current paper a direct approach is chosen.

### **Methodology**

Flux maps of solar concentrating systems are usually obtained using Lambertian targets and CCD cameras in conjunction with flux sensors for calibration [24]. A water-cooled Lambertian target is positioned at the focal plane. A highly linear digital camera is then used to acquire an image of the irradiated target. The brightness of each pixel of the resulting digital image is proportional to the radiative flux incident at the pixel location. Ulmer et al. detail a flux mapping system installed at the Plataforma Solar de Almeria in Spain [24]. Similar systems have been implemented at the Paul Scherrer Institute [14] and at ETH-Zurich [2]. A flux sensor is then used to establish the relation between pixel brightness and energy flux. Multiple types of flux sensors exist. Kaluza

and Neumann have compiled a review of the various options. All directional information is lost in the diffuse reflection from the Lambertian target. Therefore, no predictions of the flux distribution on arbitrarily shaped receivers can be obtained via the flux maps. Furthermore, direct measurement of the directional distribution of radiation is impractical due to the very high flux levels in the focal region. If information about the flux distribution in multiple planes is available, it can be used to partially restore the directional information [30]. A schematic representation of a typical flux measurement setup is depicted in Figure 5-1.

### Derivation for the general case

A schematic depiction of the general, three-dimensional case of a ray originating at a solar concentrator and passing through several parallel planes is shown in Figure 5-2. Air is assumed to be a non-participating medium, reducing the RTE to

$$\frac{dI}{ds} = 0 \quad (5-1)$$

Thus, the intensity,  $I$ , is constant along any straight line. According to Figure 5-2, for a given direction  $(\theta, \varphi)$  positions of equal intensity are given by,

$$I(x, y, z, \theta, \varphi) = I_o(x_o, y_o, \theta, \varphi) = I_o(x + z \cos \varphi \tan \theta, y + z \sin \varphi \tan \theta, \theta, \varphi). \quad (5-2)$$

The flux at a given position is obtained by integrating the projected intensity over the hemisphere:

$$q''(x, y, z) = \int_{\varphi=0}^{2\pi} \int_{\theta=0}^{\frac{\pi}{2}} I(x, y, z, \theta, \varphi) \cos \theta \sin \theta d\theta d\varphi \quad (5-3)$$

Substituting the result of Equation 5-2 for the intensity in Equation 5-3 one obtains

$$q''(x, y, z) = \int_{\varphi=0}^{2\pi} \int_{\theta=0}^{\frac{\pi}{2}} I_o(x + z \cos \varphi \tan \theta, y + z \sin \varphi \tan \theta, \theta, \varphi) \cos \theta \sin \theta d\theta d\varphi \quad (5-4)$$

Equation 5-4 can then be discretized. The measured values of radiative flux,  $q''(x, y, z)$ , are known at discrete locations on a Cartesian grid defined by  $j, k, l$ :

$$q_{jkl} = q''(x_{\text{ref}} + j\Delta x_f, y_{\text{ref}} + k\Delta y_f, z_{\text{ref}} + l\Delta z_f) \quad (5-5)$$

The unknown intensity distribution in the solution plane ( $z=0$ ) is spatially discretized on a uniform rectangular grid in  $x$  and  $y$  while the directional distribution is uniform in elevation ( $\theta$ ) and azimuthal ( $\varphi$ ) angles. Equation 5-4 then becomes

$$q_{jkl} = \sum_{m=1, n=1}^{N_\theta, N_\varphi} \left[ w_x w_y I_{o, J+1, K+1, m, n} + w_x (1-w_y) I_{o, J, K+1, m, n} + (1-w_x) w_y I_{o, J+1, K, m, n} + (1-w_x)(1-w_y) I_{o, J, K, m, n} \right] \cos \theta_m \sin \theta_m \Delta \theta \Delta \varphi \quad (5-6)$$

This is a linear system of equations of the form  $\mathbf{q} = \mathbf{A}\mathbf{I}_o$ , where the radiative flux,  $\mathbf{q}$ , is known and the intensity at the solution plane,  $\mathbf{I}_o$ , is unknown. The system is further defined by Equations 5-7 through 5-9.

$$x_{o, jklmn} = x_j + z_l \cos \varphi_n \tan \theta_m, y_{o, jklmn} = y_k + z_l \sin \varphi_n \tan \theta_m \quad (5-7)$$

$$J = \text{ceiling} \left( \frac{x_{o, jklmn} - x_r}{\Delta x} \right), K = \text{ceiling} \left( \frac{y_{o, jklmn} - y_r}{\Delta y} \right) \quad (5-8)$$

$$w_x = \frac{x_{o, jklmn} - x_J}{\Delta x}, w_y = \frac{y_{o, jklmn} - y_K}{\Delta y} \quad (5-9)$$

Equations 5-7 calculate the location of intersection on the solution plane for the  $x$  and  $y$ -directions, respectively. Equations 5-8 calculate the index of intersection on the solution plane in the  $x$  and  $y$  directions. Equations 5-9 calculate the weighting factors in the  $x$  and  $y$ -directions as intersections will always occur between two nodal points. The fully three-dimensional case is presented for completeness but is not yet successfully implemented and therefore no results are available.

## Two dimensional case

The high dimensionality of the intensity distribution on the solution plane in the most general case (two spatial and two directional coordinates) leads to very large

systems of equations. Therefore an important subclass of problems, the purely two-dimensional case, is explored in detail. The 2D situation is applicable to concentrators such as parabolic, elliptical, and circular troughs and 2D compound parabolic concentrators (CPC's). Figure 5-3 depicts the flux distribution at varying locations on the focal axis of a 2D concentrator.

The derivation of the 2D case is analogous to that of the 3D case. The intensity at an arbitrary position and direction  $(x, y, \theta)$  can be related to the intensity in the solution plane according to

$$I(x, y, \theta) = I_o(x + z \tan \theta, \theta) \quad (5-10)$$

The radiative flux incident at a given location,  $q''(x, z)$ , is calculated from the intensity according to the two-dimensional equivalent of Equation 5-4.

$$q''(x, z) = \int_{\theta=-\frac{\pi}{2}}^{\frac{\pi}{2}} I(x, z, \theta) \cos \theta d\theta = \int_{\theta=-\frac{\pi}{2}}^{\frac{\pi}{2}} I_o(x + z \tan \theta, \theta) \cos \theta d\theta \quad (5-11)$$

Discretization of Equation 5-11 leads to

$$q_{jl} = \sum_{m=1}^{N_\theta} \left( (1 - w_x) I_{0,J,m} + w_x I_{0,J+1,m} \right) \cos \theta_m \Delta \theta \quad (5-12)$$

In Equation 5-12,  $q_{j,l}$  represents the radiative flux at location  $j$  on plane  $l$ . Using the 2D equivalents of Equations 5-7, 5-8, and 5-9, the weighting factor  $w_x$  is found. The intensity,  $I_{0,J,m}$ , is the intensity in direction  $m$  at location  $J$  on the solution plane.

### Circular Symmetric case

Many optical concentrators are circularly symmetric. In these cases, the intensity in the focal plane depends on three independent variables: the radial position,  $r$ , and two directional angles,  $\theta$  and  $\varphi$ . In contrast, the general case requires four independent

variables. A system consisting of a circular concentrator and a plane circular target is considered.

From Figure 5-4 one obtains the geometrical relationship between the radial position and direction  $(r, \theta, \varphi)$  in any plane  $z$  to a position and direction on the solution plane  $(r_o, \theta, \varphi_o)$ .

$$r_o = r^2 + (z \tan \theta)^2 - 2rz \tan \theta \cos(\pi - \varphi) \quad (5-13)$$

$$\varphi_o = \cos^{-1} \left( \frac{r_o^2 - r^2 + (z \tan \theta)^2}{2r_o z \tan \theta} \right) \quad (5-14)$$

Note that the elevation angle,  $\theta$ , remains unchanged. As for the general case, the intensity along a straight line is constant leading to

$$q''(r, z) = \int_{\varphi=0}^{2\pi} \int_{\theta=0}^{\frac{\pi}{2}} I_o(r_o, \theta, \varphi_o) \cos \theta \sin \theta d\theta d\varphi \quad (5-15)$$

The flux distribution  $q''(r, z)$  is known from measurement or ray-tracing simulations using

$$q_{j,l} = q''(j\Delta r_f, z_{ref} + l\Delta z_f) \quad (5-16)$$

discretization then yields

$$q_{j,l} = \sum_{m=1, n=1}^{N_\theta, N_\varphi} \left[ (1-w_\varphi)(1-w_r)I_{o,J,m,N} + (1-w_\varphi)w_r I_{o,J+1,m,N} \right. \\ \left. + (1-w_r)w_\varphi I_{o,J,m,N+1} + (1-w_r)(1-w_\varphi)I_{o,J+1,m,N+1} \right] \cos \theta_m \sin \theta_m \Delta\theta \Delta\varphi \quad (5-17)$$

where

$$J = \text{ceiling} \left( \frac{r_o - \frac{dr}{2}}{dr} \right), N = \text{ceiling} \left( \frac{\varphi_o - \frac{d\varphi}{2}}{d\varphi} \right) \quad (5-18)$$

$$w_r = \frac{r_o - r_J}{dr}, w_\varphi = \frac{\varphi_o - \varphi_N}{d\varphi} \quad (5-19)$$

## Regularization

Inverse radiation problems often suffer from ill-conditioned coefficient matrices [40]. For continuous solutions, Tikhonov regularization can be employed to impose smoothness onto the solution [41]. It is implemented by appending a matrix to the  $A$  matrix for each discretization variable. These matrices are carefully chosen to implement desired constraints on the system. For the inverse method, a smoothness constraint is applied due to prior knowledge about the intensity distribution. This method is controlled via one regularization parameter per dimension of the unknown quantity ( $\lambda_x$  and  $\lambda_\theta$  in the two-dimensional case). Parameter values of zero correspond to the non-regularized solution while parameter values greater than zero increase the effect of the regularization.

## Monte Carlo Ray Tracing

An in-house Monte Carlo ray tracing program [23] is used to model the concentrating systems. The program features directional binning, which allows for the output of the intensity distribution at any desired location. The program provides the intensity distribution as well as the consistent, associated flux distribution, allowing for in-depth validation of the inverse method.

## Results

### Parabolic Trough

Parabolic troughs are the most common 2D concentrators (Figure 5-5). The EuroTrough 150 (ET-150) [26], which was developed under European Commission Project EuroTrough II (5<sup>th</sup> Framework Program contract number ERK6-CT-1999-00018), was modeled using the Monte Carlo ray tracing code [23]. A Gaussian error of 5 mrad is introduced at the reflector surface to account for manufacturing and other errors. A

larger mirror error corresponds to a larger area of concentration with lower maximum flux levels. Mirror error can be modified to make the calculated flux distribution closely match that of an actual concentrator setup.

The flux distributions in the focal plane and the associated intensity distributions are shown in Figures 5-6 and 5-7. The highest intensity values are found at the center of the target, where the concentration is the highest, while the intensity diminishes as the angle of incidence ( $\theta$ ) increases. The flux diminishes as one moves away from the focal plane ( $z^*=0.0$ ).

The inverse method features a range of parameters that influence the accuracy of the solution. These parameters include the number of discretization steps in both the  $\theta$  and x-direction ( $N_{x0}$  and  $N_{\theta}$ ) and the length of the solution plane ( $L_{x0}$ ). A range of parameter values was set based on the desired resolution of the solution. The inverse solution was generated for each possible combination of parameter values. Solutions were compared based on the RMS difference between each inverse and Monte Carlo solution with the lowest value corresponding to the optimal solution.

Figure 5-8 shows the inverse solution based on the flux distributions from Figure 5-6. The inverse solution results closely match the Monte Carlo solutions. The discontinuity at larger angles of incidence is reproduced by the inverse solution. The largest discrepancies between inverse and Monte Carlo solutions are concentrated around areas with large gradients and discontinuities in the intensity. The optimal parameters for the parabolic trough were found to be  $N_{\theta}=15$ ,  $N_{x0}=20$  and  $L_{x0}=0.12$  m. The inverse solution has a maximum error of 9% with a RMS relative error of 3.1%. The linear system is of full rank with a characteristic number of 1000. Tikhonov

regularization did not improve results. This is attributed to the discontinuous nature of the solution.

### **Elliptical Trough**

An elliptical trough-based Vortek-type linear concentrator set-up [2] is studied. The set-up (Table 5-2, Figure 5-9) consists of an Argon long arc lamp, an elliptical trough reflector and a cylindrical mirror on the underside of the arc. Secondary mirrors are attached at the outlet of the elliptical trough to reduce losses.

The flux and intensity distributions from Monte Carlo ray tracing are shown in Figures 5-10 and 5-11. The inverse solution is shown in Figure 5-12. The optimal parameters for the elliptical trough were found to be  $N_\theta=5$ ,  $N_{x_0}=41$  and  $L_{x_0}=0.41$  m. The solution has a maximum error of 18% with an RMS relative error of 5.1%. Tikhonov regularization significantly improves the results in the elliptical trough case. The optimal values for the Tikhonov coefficients are  $\lambda_\theta=5$  and  $\lambda_x=12$ . The condition number of the regularized linear system is 16.4.

### **Conclusions**

An inverse solution method to identify intensity distributions at the focal plane of two-dimensional concentrating systems has been developed. The method uses multiple flux maps perpendicular to the concentrator axis to predict the intensity distribution in the focal plane. The mathematical derivation of the circular symmetric and general, three-dimensional cases has been presented. A parabolic trough setup was explored using an in-house Monte Carlo ray-tracing program. The optimal discretization parameters for this setup were found to be  $N_\theta=15$ ,  $N_{x_0}=20$ , and  $L_{x_0}/f=0.0702$ . The results show that the inverse solution process can be applied to a set of two-dimensional flux measurements to successfully predict the intensity distribution.

The maximum relative error was less than 10% with an RMS relative error of 3.1%. Furthermore, an elliptical trough setup was also implemented. Tikhonov regularization was used to overcome ill-conditioning of the problem. The elliptical trough solution was optimal for discretization parameter  $N_\theta=5$ ,  $N_{x_0}=41$ , and  $L_{x_0}=1.7559$  and Tikhonov parameters  $\lambda_\theta=5$  and  $\lambda_x=12$  resulting in a relative error of less than 18% and corresponding RMS relative error of 5.1%. In the parabolic trough case Tikhonov regularization has a negative effect due to the discontinuous nature of the solution.

### **Least Squares Constraints**

MATLAB provides a large toolbox to aid in the solution of ill conditioned **A** matrices. The “lsqin” command provides many options for constraining the solution to a least squares problem. It includes the capability of providing an upper and lower bound. A lower bound of zero is easily applied to the inverse problem because the intensity must be positive or zero. An upper limit can be applied to improve results but also increases computation time. The “lsqin” solver also has other functions that can be implemented to improve solution accuracy such as the ability to define known intensities. This is advantageous for areas where the intensity is known to be zero due to rim angle calculations.

### **Alternative Methods**

The difficulties of implementing the fully 3D case lead us to explore other options for identifying the intensity distribution. Through the use of cameras, intensity distributions can be directly measured. Two methods of measurement are presented.

#### **Direct Measurement**

First and foremost, intensities can be measured directly at a single point using a camera. Cameras are, in fact, intensity measurement devices. In its most basic form, a

camera consists, of a cavity with a small aperture and a detection device at the backplane of the cavity (Figure 5-13). The perpendicular distance between the backplane and the aperture is the focal length,  $f$ . Lenses are used to increase the amount of light that is channeled through the aperture. The CCD chip of the camera typically returns an integer gray value,  $\psi_{ij}$ , proportional to the flux,  $q_{ij}$ , incident on pixel  $i$ ,  $j$ , where  $i$  is the number of the pixel in the horizontal axis of the chip and  $j$  is the number of the pixel in the vertical axis of the chip.

$$q_{ij} = c\psi_{ij} \quad (5-20)$$

In Equation 5-20,  $c$  represents a device dependent proportionality constant.

According to the definition of intensity

$$Q_{ij} = q_{ij}dA = I_{ij}d\Omega dA_p = I_{ij}d\Omega \cos \theta dA \cong I_{ij}\Delta\Omega_{ij} \cos \theta \Delta A \quad (5-21)$$

Therefore

$$I_{ij} = I(\theta_{ij}, \phi_{ij}) = \frac{c\psi_{ij}}{\Delta\Omega_{ij} \cos \theta_{ij}} \quad (5-22)$$

The system is further characterized by Equations 5-23 through 5-28.

$$x_i = i\Delta x \quad (5-23)$$

$$y_j = j\Delta y \quad (5-24)$$

$$\Delta A = \Delta x \Delta y \quad (5-25)$$

$$S_{ij}^2 = x_i^2 + y_j^2 + f^2 \quad (5-26)$$

$$\cos \theta_{ij} = \frac{f}{S_{ij}} \quad (5-27)$$

$$\Delta\Omega_{ij} = \frac{\Delta A \cos \theta_{ij}}{S_{ij}^2} \quad (5-28)$$

While providing superior precision and resolution, the direct method suffers from two drawbacks. First, for very high fluxes like those typically encountered in concentrating solar applications the camera must be protected by a reflective filter.

Alternatively, the camera can be positioned a sufficient distance away from the focal plane such that the flux levels are too low to harm the equipment. Secondly, the camera measures the average directional intensity distribution in the aperture. In order to identify the desired intensity distribution, i.e., at multiple points, the camera must be accurately positioned in a two-dimensional plane. Then, a measurement is taken at every point of a rectangular grid. The accurate positioning of the camera is significantly more complex than the z-positioning of a flux target.

### **Aperture Method**

The aperture method is an approach that solves one of the main problems with the direct measurement method. The experimental setup is depicted in Figure 5-14. Similar to the direct measurement method, the intensity can be identified directly. However, the camera is not directly exposed to high flux levels. While the apparatus can be positioned close to the focal plane reducing the traveling distance, it still must be accurately positioned on a two dimensional grid.

Table 5-1. Parameters of the parabolic trough.

Parameter	Value
Focal length (m)	1.71
Rim angle (°)	60.0
Sun Shape (mrad)	4.649
Mirror Error (mrad)	5.0
Mirror Reflectivity (-)	0.95

Table 5-2. Elliptical trough parameters

Parameter	Value
Semi-major Axis, $a$ (m)	0.277
Semi-minor Axis, $b$ (m)	0.190
Sun Shape (mrad)	4.649
Mirror Error (mrad)	5.0
Mirror Reflectivity (-)	0.90
Collector Length (m)	100

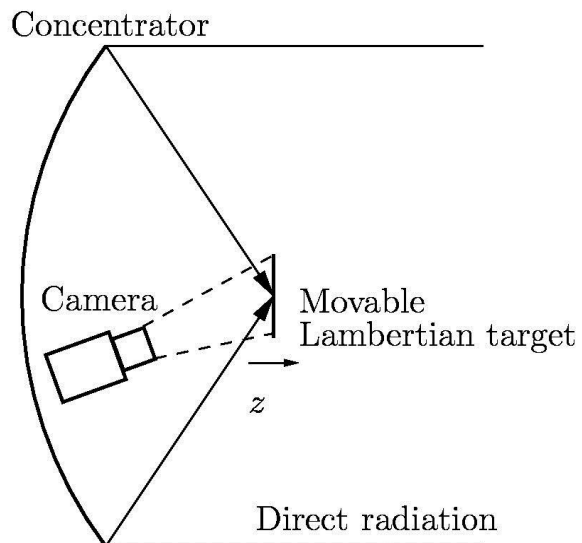


Figure 5-1. Flux mapping setup.

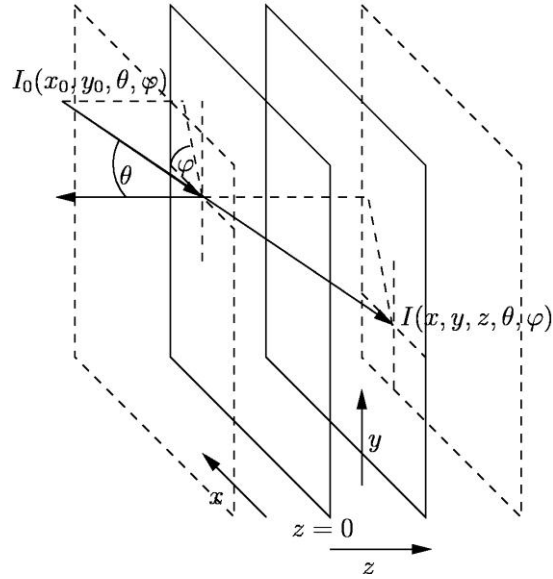


Figure 5-2. General case of a ray passing through multiple flux planes and the solution plane (at  $z=0$ ).

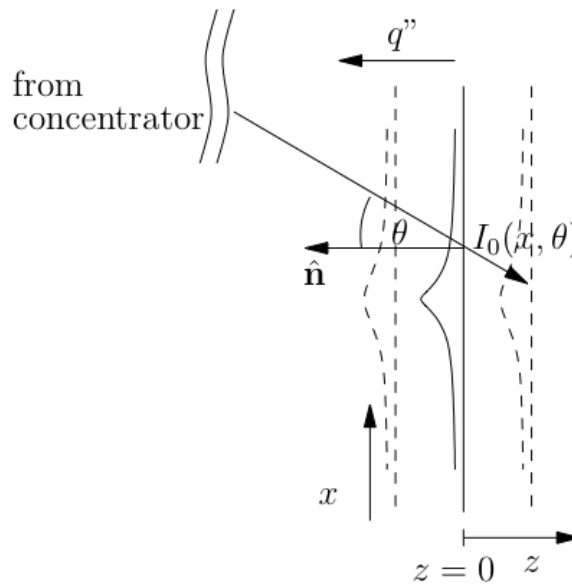


Figure 5-3. Two-dimensional flux maps.

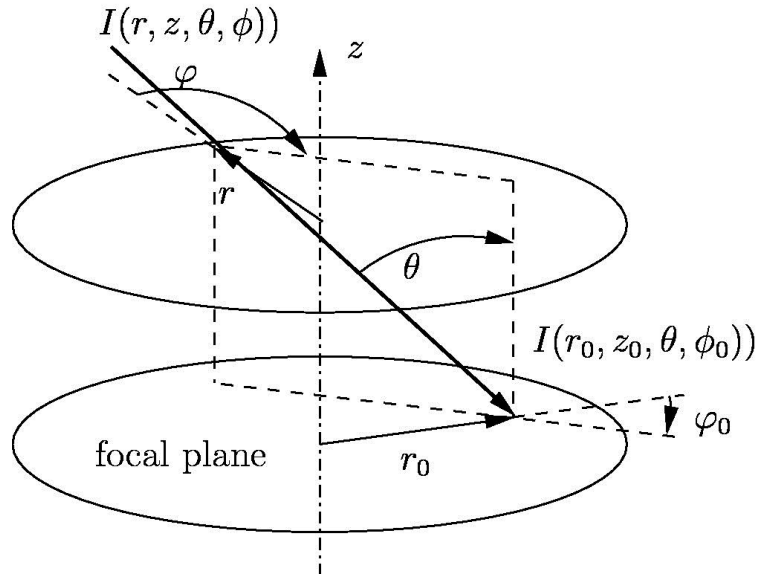


Figure 5-4. Schematic representation of the circular symmetric case.

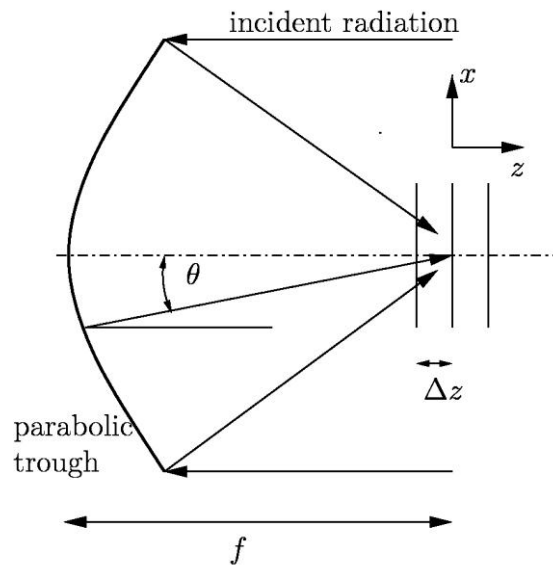


Figure 5-5. 2D parabolic trough as modeled in VeGaS. The useable output from the model is the intensity distribution on the target.

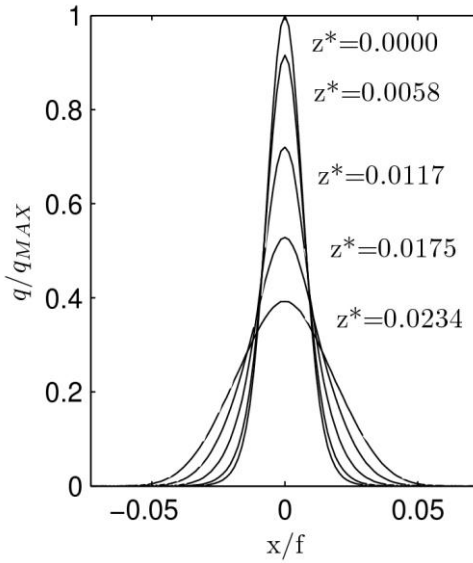


Figure 5-6. Parabolic trough scaled flux distribution at multiple distances ( $z^*=z/f$ ) from the focal plane.

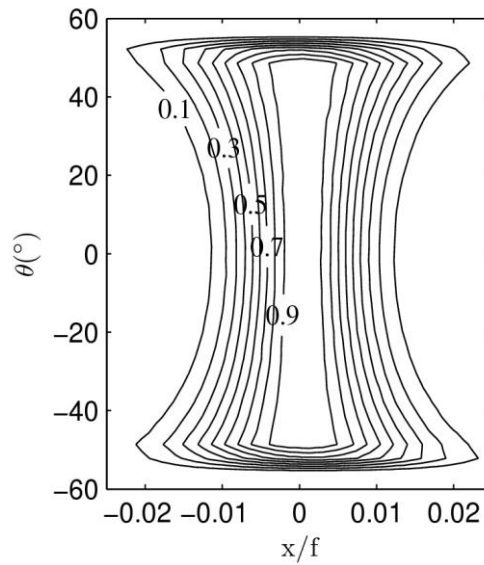


Figure 5-7. Scaled intensity distribution ( $I/I_{max}$ ) along the focal plane of a 2D parabolic trough from Monte Carlo ray tracing.

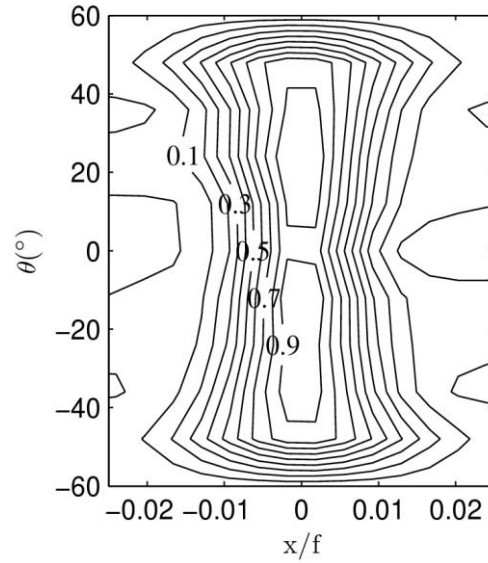


Figure 5-8. Scaled inverse solution results ( $I/I_{max}$ ) at the focal plane ( $z^*=0.0$ ).  $N_\theta = 15$ ,  $N_{x_0} = 20$   $L_{x_0} = 0.12$  m.

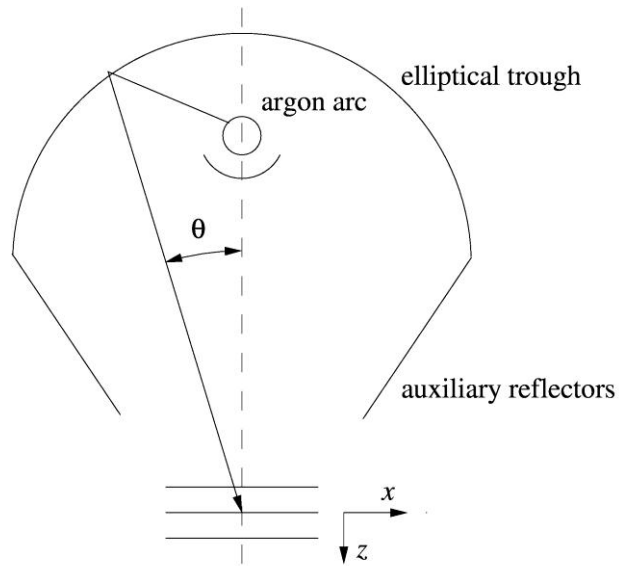


Figure 5-9. Schematic representation of the elliptical trough setup as implemented in Vegas.

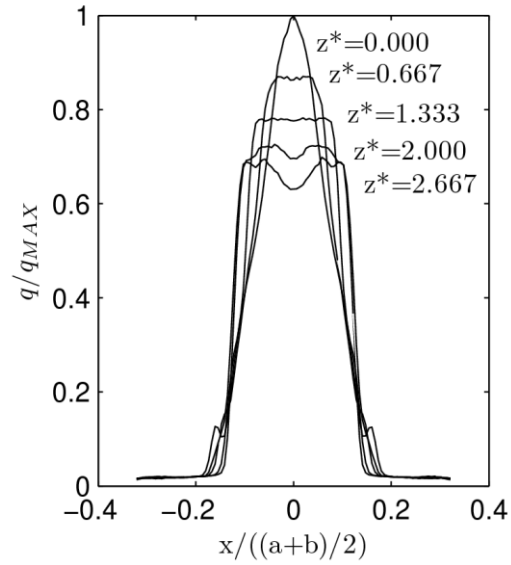


Figure 5-10. Scaled flux distribution at varying distances ( $z^*=z/((a+b)/2)$ ) from the parabolic trough.

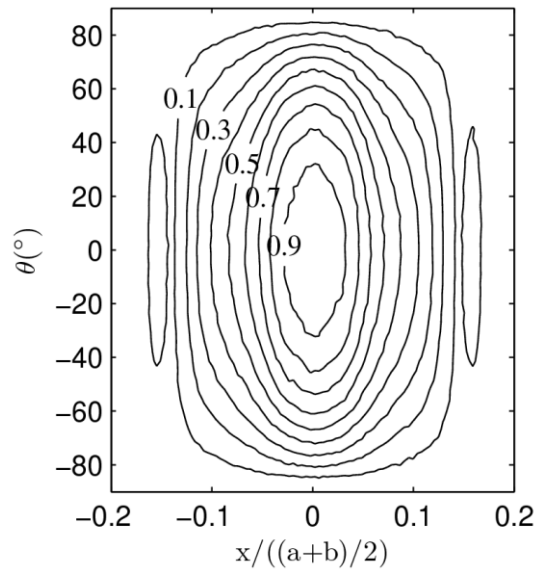


Figure 5-11. Scaled intensity distribution along the focal plane of a 2D parabolic trough from Monte Carlo ray tracing.

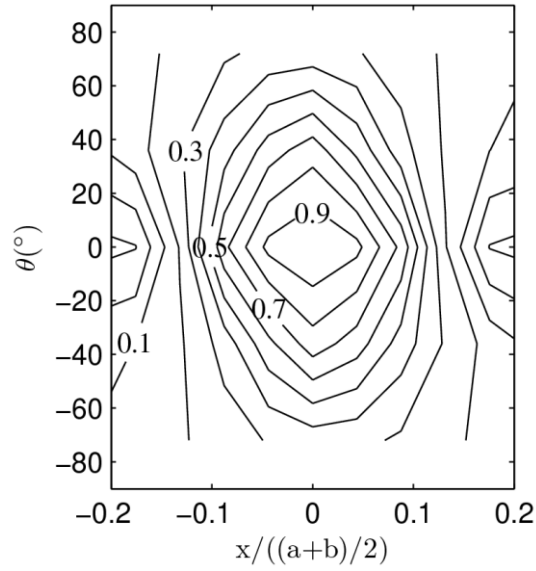


Figure 5-12. Scaled inverse solution results ( $\|I_{\max}$ ) at the focal plane ( $z^*=0.0$ ).  $N_{\theta} = 5$ ,  
 $N_{x_0} = 41$   $L_{x_0} = 0.41$  m,  $\lambda_x = 12$   $\lambda_{\theta} = 5$ .

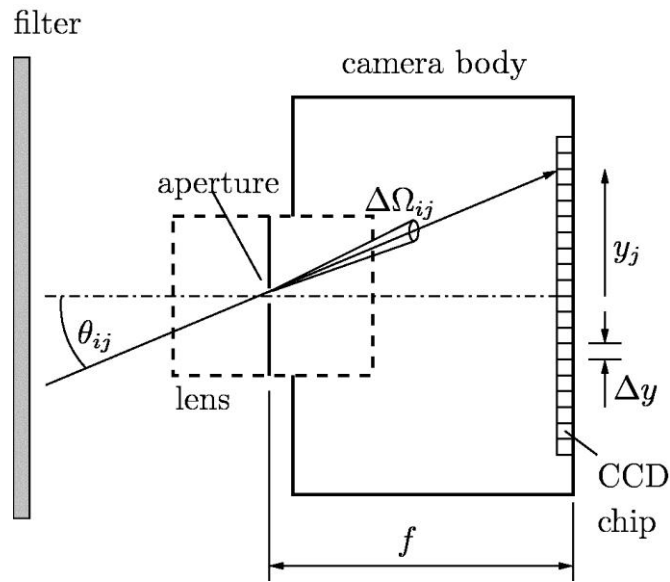


Figure 5-13. Camera as an intensity measurement device.

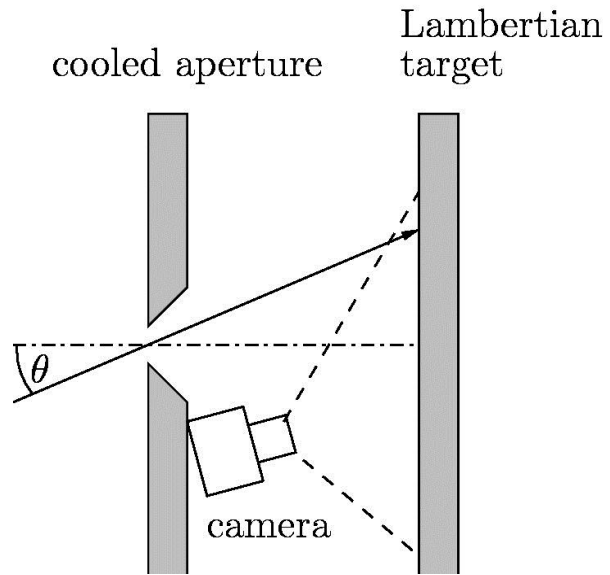


Figure 5-14. Schematic diagram showing a potential setup for implementing the aperture method.

## CHAPTER 6 CONCLUSIONS

### Summary

A high heat flux solar simulator was designed, built and operated on the campus of the University of Florida. The simulator has been fully described, including all necessary subsystems. These subsystems provide the flexibility required to run a multitude of experiments in the future. They include the XY table, flux target, camera/MATLAB integration and data acquisition subsystems. The simulator system has generated flux levels as high as  $4230 \text{ kW/m}^2$ , which corresponds to black body stagnation temperatures of approximately 2942 K. It will be used for high temperature solar research such as phase change energy storage and thermochemical methods for energy generation.

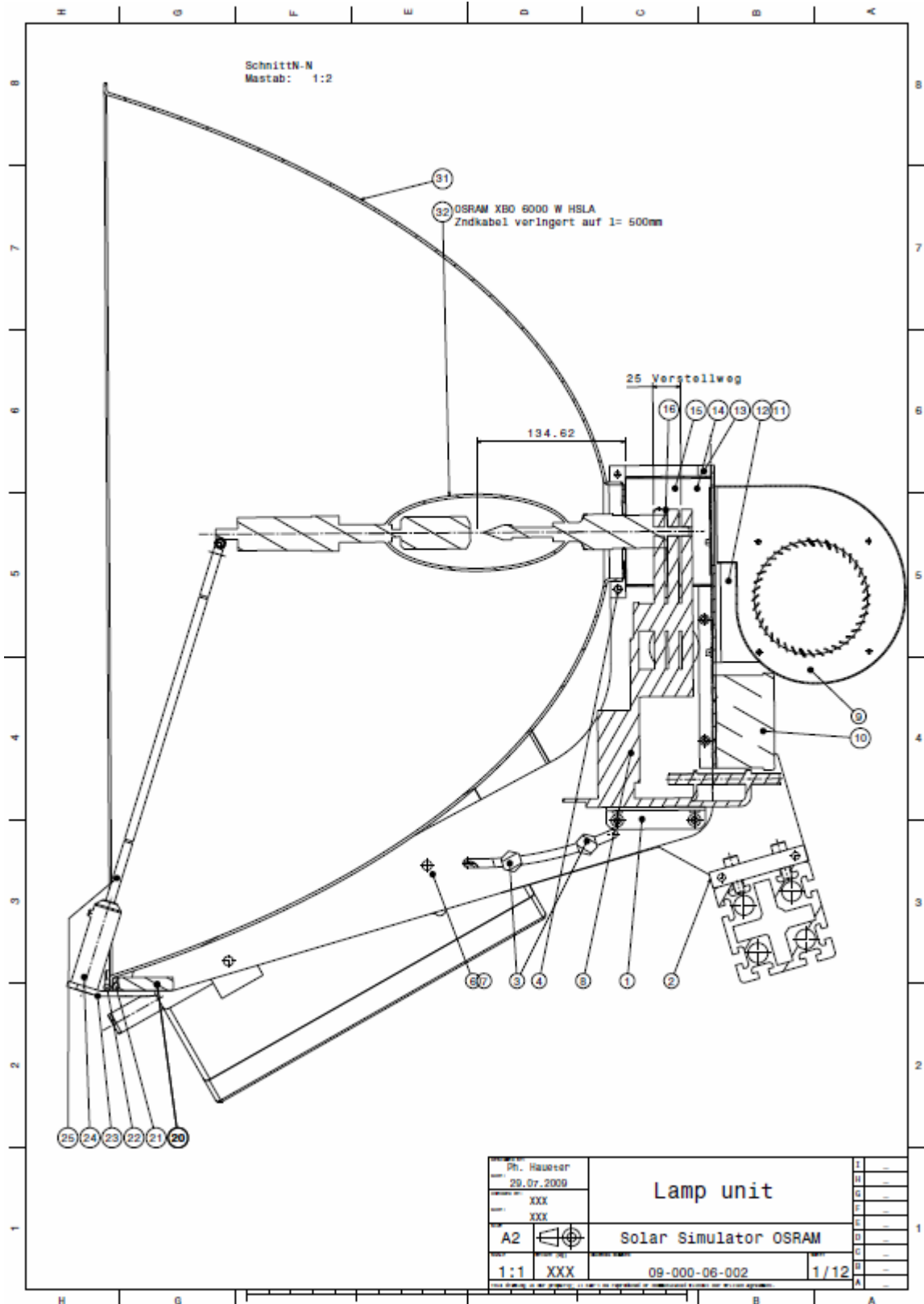
An inverse solution method to calculate intensity distributions at the focal plane of two dimensional concentrating systems was presented. The method uses multiple flux maps along the concentration axis of a concentrating setup to predict the intensity distribution and the focal plane. The mathematics for the fully three dimensional and circular symmetric cases has been presented but not yet implemented. A parabolic and elliptical trough setup was explored using the in-house Monte Carlo ray tracing program. The optimal parameters for the parabolic trough were found to be  $N_\theta=15$ ,  $N_{x\theta}=20$ , and  $L_{x\theta}=0.12$  meters. The results show that the inverse solution process can be applied to a set of flux measurements to successfully predict the intensity distribution with a relative error of less than 10%. Tikhonov regularization was on the elliptical trough case to aid in solving for a distribution that was assumed to have a smooth solution. The elliptical trough solution was optimized with the parameters  $N_\theta=5$ ,  $N_{x\theta}=41$ ,  $L_{x\theta}=0.41$

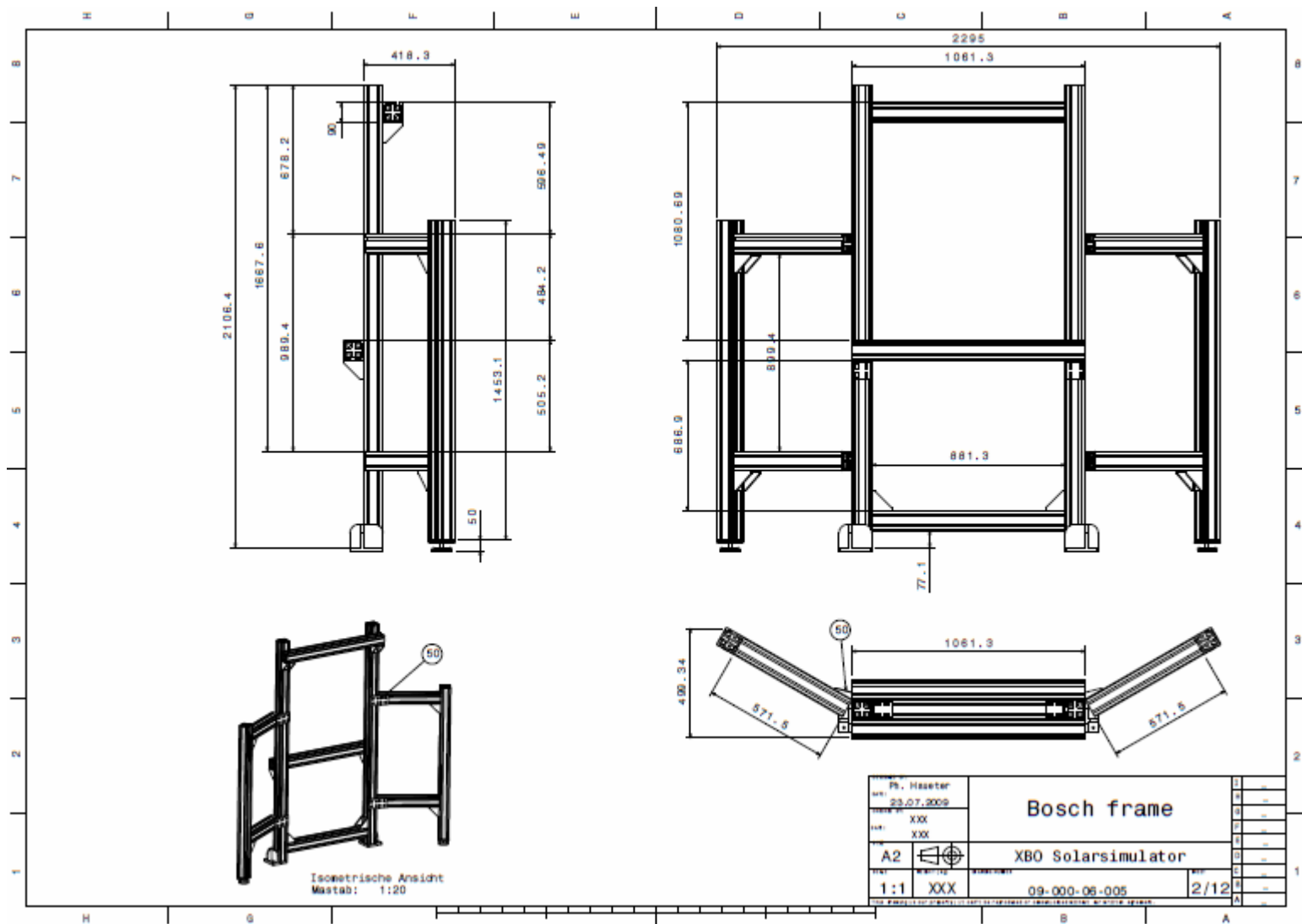
meters,  $\lambda_\theta=5$ , and  $\lambda_x=12$  resulting in a relative error of less than 18%. In contrast with the elliptical trough case, in the parabolic trough case it is evident that Tikhonov regularization has a negative effect when sharp changes in the intensity distribution are present. The success with the two dimensional case suggests the three dimensional case may be possible. However, the high dimensionality of the fully three dimensional case causes many rank deficiency issues.

### **Outlook**

Looking forward, refinement of the circular symmetric case is the logical next step. The case has shown some promise in initial testing but does begin to suffer from rank deficiency issues. After successfully implementing the circular symmetric case, the next step is to work on the fully three dimensional case. The high dimensionality of this problem poses many issues and will require some inventive manipulation to get a reasonable answer. In addition, a method for coherently plotting the results will need to be developed. A code designed to take the output intensity from the inverse problem and apply it to designed receiver geometries would be useful. This would allow the experimentalist to effectively design reactors for specific concentrating systems. The solar simulator will be used for high temperature experiments for the foreseeable future. It allows the University of Florida to be at the forefront of the push towards sustainable energy research.

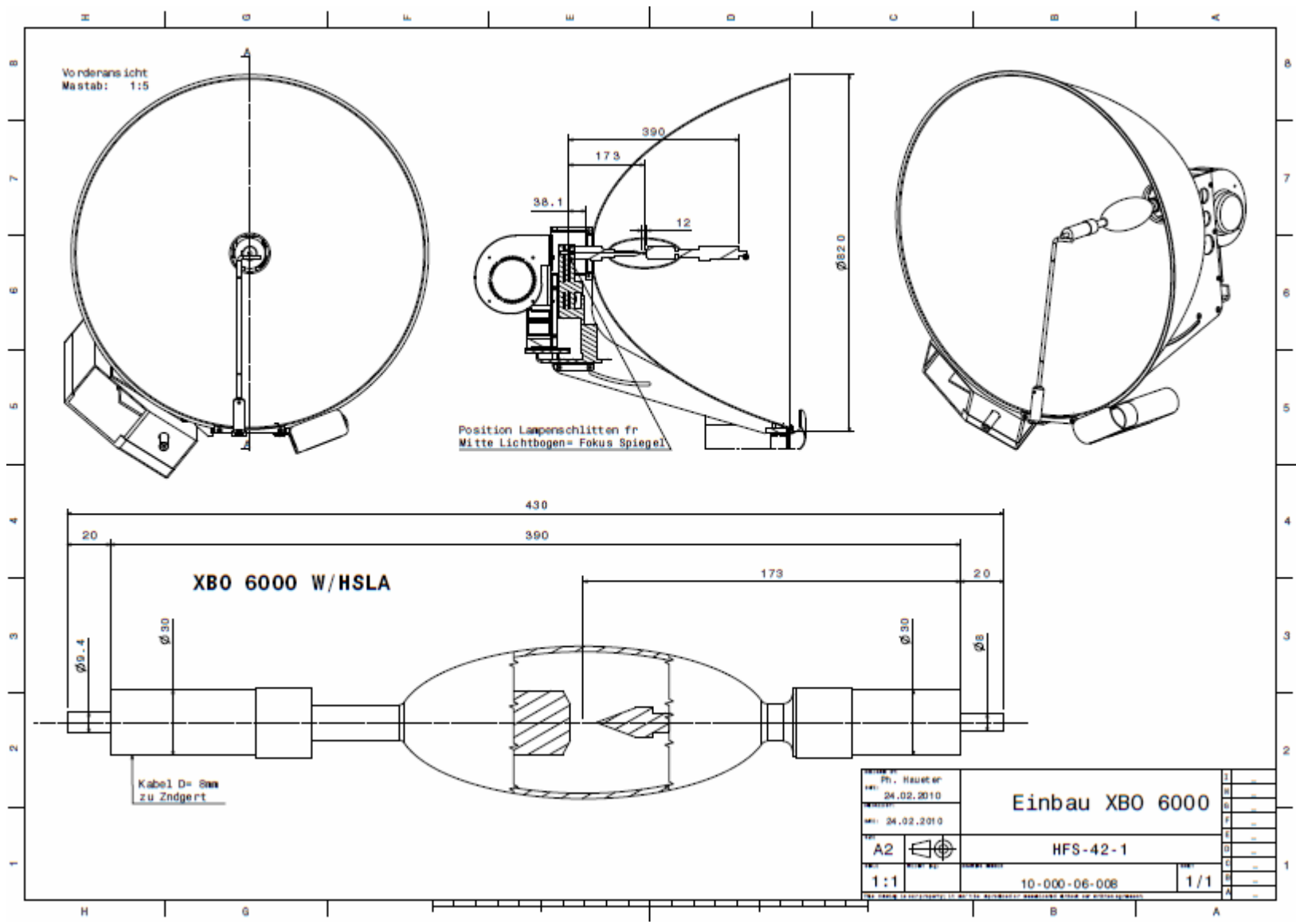
# APPENDIX A SIMULATOR DRAWINGS

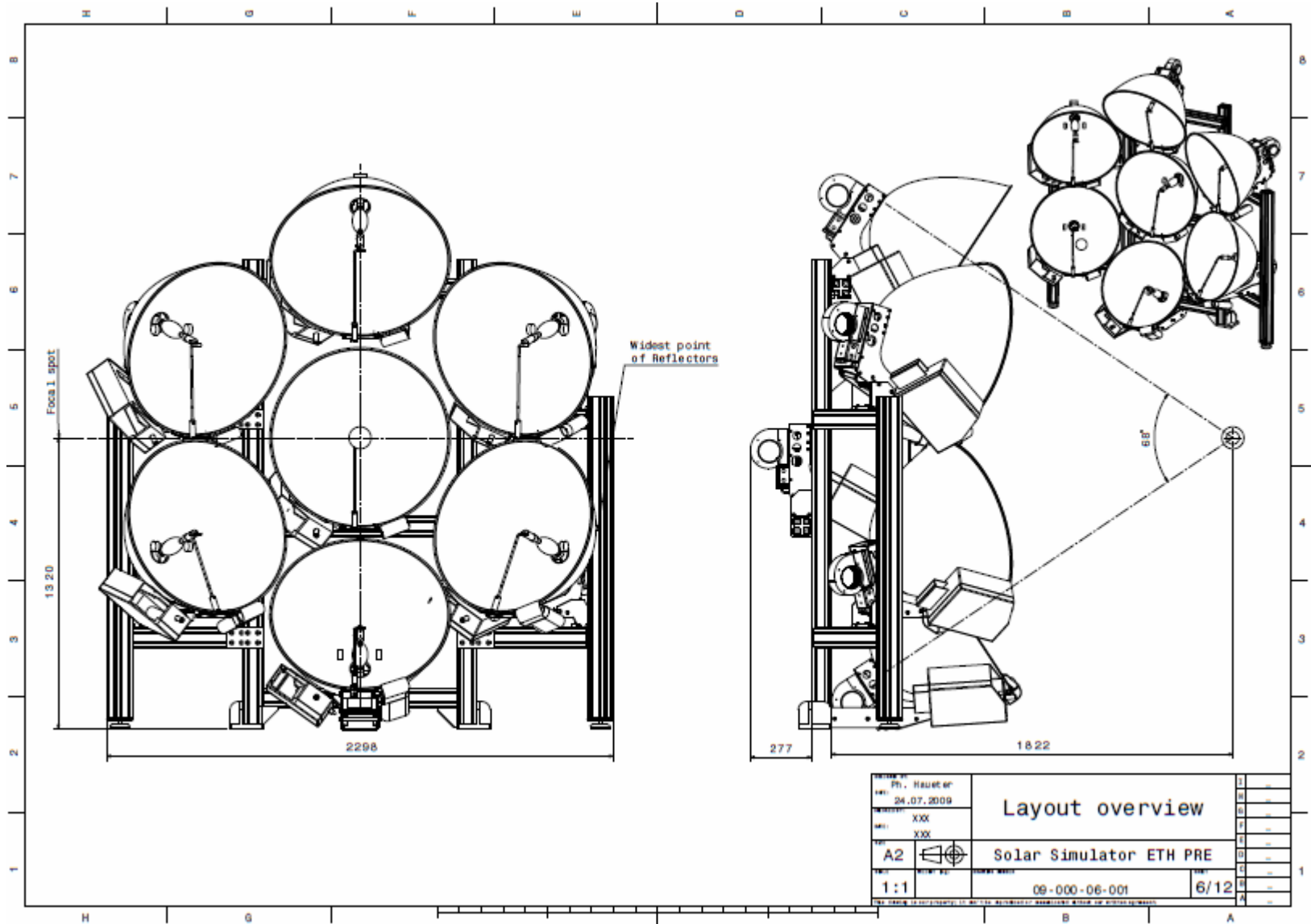


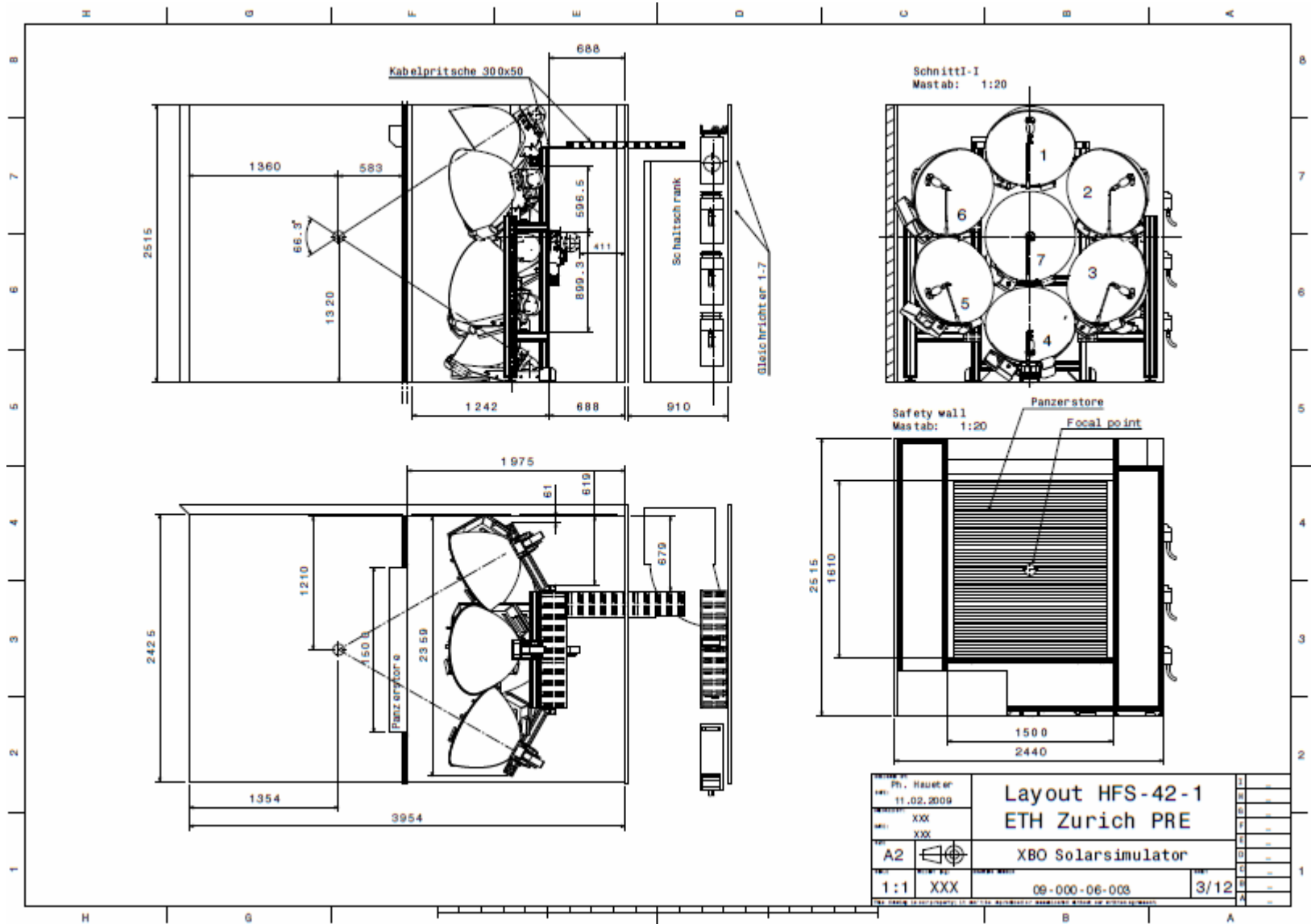




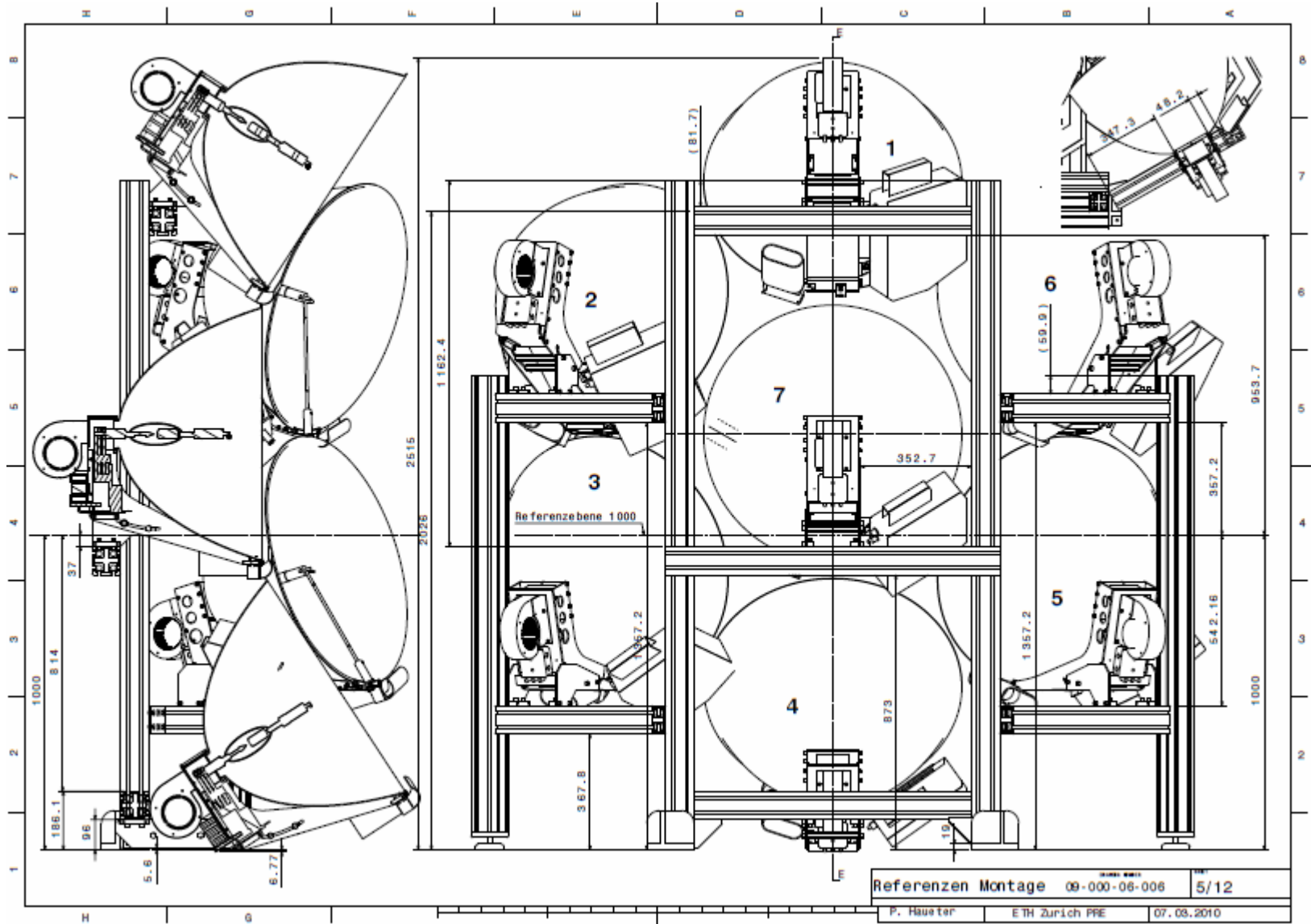


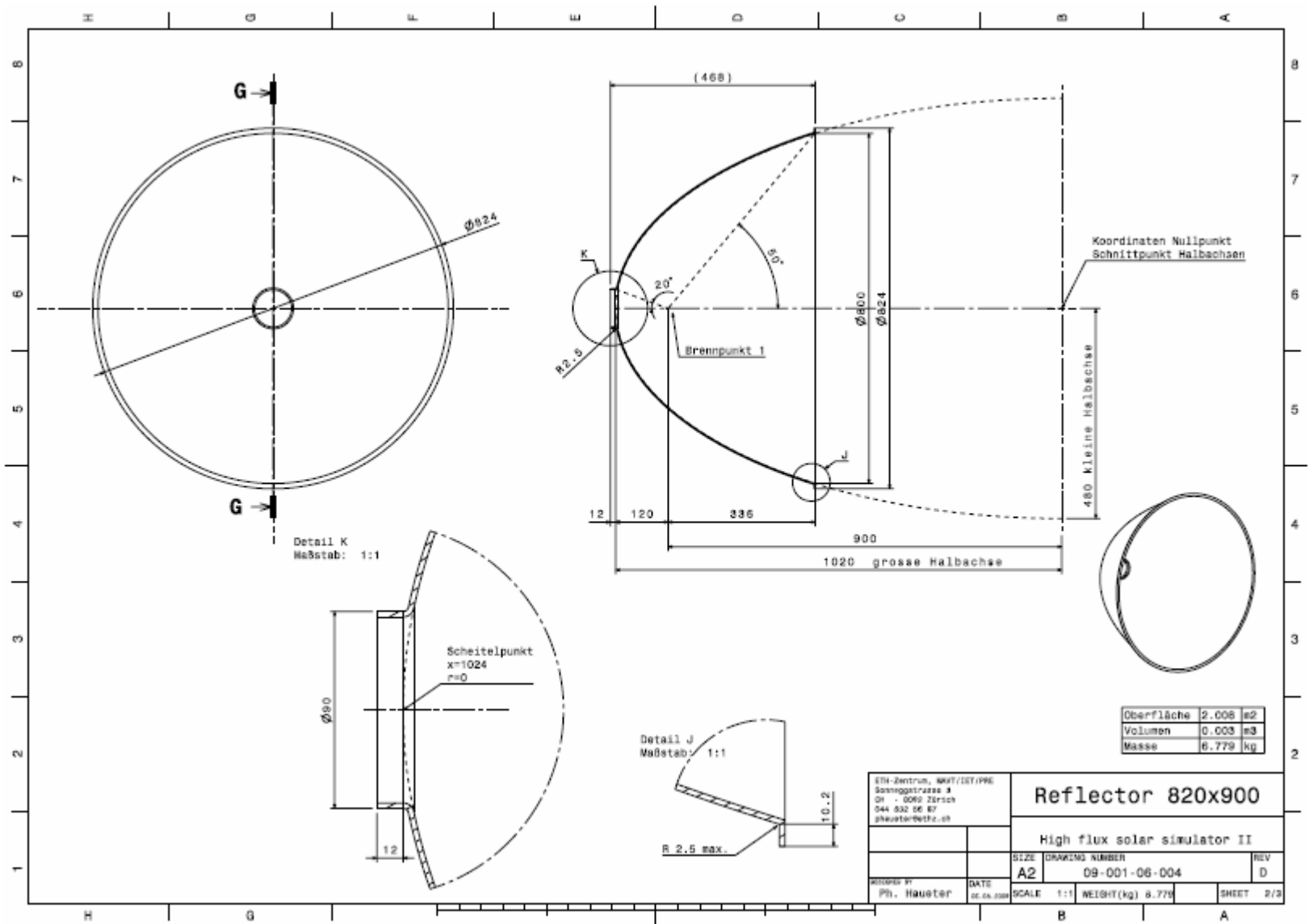


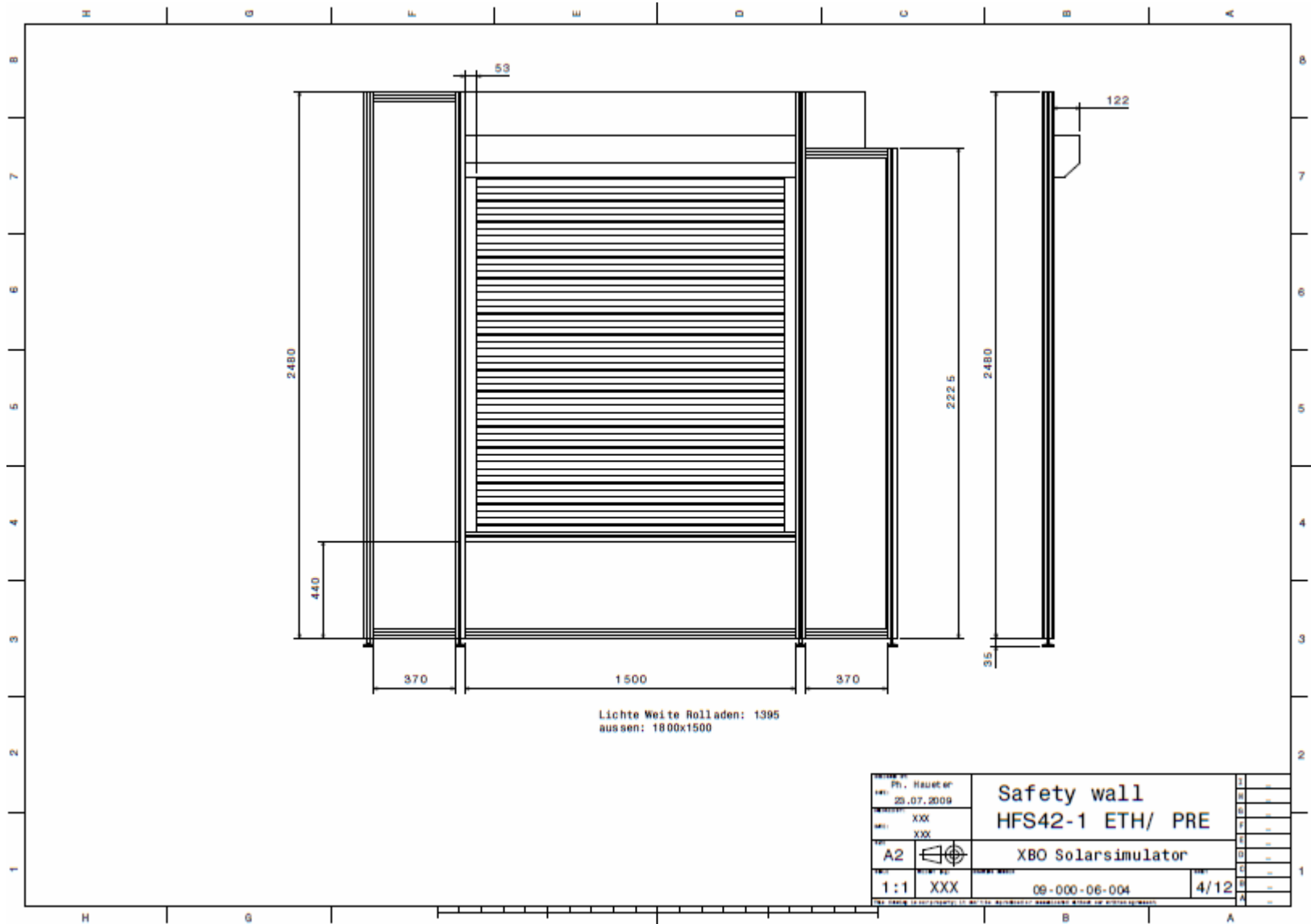




Proj. No.	Rev. No.	Layout HFS-42-1		1
11.02.2009		ETH Zurich PRE		2
XXX		XBO Solarsimulator		3
XXX				4
A2				5
1:1	XXX	09-000-06-008	3/12	6
<small>© 2009 ETH Zurich. All rights reserved. ETH Zurich is not responsible for any damage or injury caused by the use of this document.</small>				7
				8







**Kommentar***Inhalt**Autor**Letzte Änderung***Input**

Spiegel Radius (m)

0.4

c: Halber Fokusabstand (m)

0.9

Öffnungswinkel (°)

50

**Zwischenresultate**

Öffnungswinkel (rad)

0.8728648

x (m)

0.5643601

Parameter quad. Gln.

a	b	c
1	-1.2885	0.257987

D: Determinante quad. Gln.

0.6282907

a<sup>2</sup>

1.0405751

b<sup>2</sup>

0.2305751

**Output**

a: Grosser Halbdurchmesser (m)

1.0200858

b: Kleiner Halbdurchmesser (m)

0.4801824

h: Tiefe des Spiegels (m)

0.4557257

ff: Abstand Spiegelrand-Fokusebene (m)

1.4643601

h-a

-0.5643601

**Farbcode**

Input: anpassen

Zwischenresultate: nicht verändern

Endresultate: nicht verändern

Berechnung von Ellipsenparametern für Reflektoren

Jörg Petrasch

06.05.2009

**Kommentar**

- 1) Bitte beachten, ob die Anzahl Zeilen ausreicht, falls nicht: x und r Werte weiter nach unten ziehen
- 2) x und r Achse sind nicht unbedingt richtig skaliert

Input

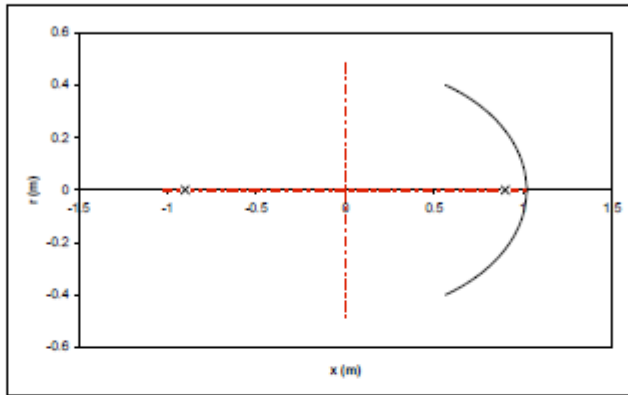
dx (m) 0.005

Output

Spiegel

Spiegel			Fokl		Kleine Halbachse		Grosse Halbachse	
x (m)	r (m)	r2 (m)	x (m)	r (m)	x (m)	r (m)	x (m)	r (m)
0.56436	0.4	-0.4	-0.9	0	-1.02009	0	0	0.480182
0.56936	0.398427	-0.39843	0.9	0	1.020086	0	0	-0.48018

0.57436	0.396833	-0.39683
0.57936	0.39522	-0.39522
0.58436	0.393585	-0.39359
0.58936	0.39193	-0.39193
0.59436	0.390253	-0.39025
0.59936	0.388555	-0.38855
0.60436	0.386835	-0.38683
0.60936	0.385093	-0.38509
0.61436	0.383328	-0.38333
0.61936	0.381541	-0.38154
0.62436	0.379731	-0.37973
0.62936	0.377898	-0.37779
0.63436	0.376041	-0.37604
0.63936	0.37416	-0.37416
0.64436	0.372254	-0.37225
0.64936	0.370324	-0.37032
0.65436	0.368369	-0.36837
0.65936	0.366388	-0.36639
0.66436	0.364381	-0.36438
0.66936	0.362348	-0.36235
0.67436	0.360288	-0.36029
0.67936	0.3582	-0.3582
0.68436	0.356085	-0.35608
0.68936	0.353941	-0.35394
0.69436	0.351769	-0.35177
0.69936	0.349567	-0.34957
0.70436	0.347336	-0.34734
0.70936	0.345073	-0.34507
0.71436	0.342778	-0.34278
0.71936	0.340455	-0.34046
0.72436	0.338098	-0.3381
0.72936	0.335708	-0.33571
0.73436	0.333284	-0.33328
0.73936	0.330825	-0.33083
0.74436	0.328331	-0.32833
0.74936	0.325801	-0.3258
0.75436	0.323234	-0.32323
0.75936	0.32063	-0.32063
0.76436	0.317986	-0.31799
0.76936	0.315303	-0.3153
0.77436	0.312579	-0.31258
0.77936	0.309813	-0.30981
0.78436	0.307005	-0.307
0.78936	0.304152	-0.30415
0.79436	0.301253	-0.30125
0.79936	0.298308	-0.29831
0.80436	0.295315	-0.29532
0.80936	0.292273	-0.29227
0.81436	0.289179	-0.28918
0.81936	0.286032	-0.28603
0.82436	0.282831	-0.28283
0.82936	0.279573	-0.27957
0.83436	0.276257	-0.27626
0.83936	0.27288	-0.27288
0.84436	0.26944	-0.26944
0.84936	0.265935	-0.26593
0.85436	0.262362	-0.26236
0.85936	0.258718	-0.25872
0.86436	0.255001	-0.255
0.86936	0.251206	-0.25121
0.87436	0.247331	-0.24733
0.87936	0.243371	-0.24337
0.88436	0.239323	-0.23932
0.88936	0.235182	-0.23518
0.89436	0.230942	-0.23094
0.89936	0.226599	-0.2266
0.90436	0.222145	-0.22215
0.90936	0.217576	-0.21758
0.91436	0.212882	-0.21288
0.91936	0.208055	-0.20806
0.92436	0.203087	-0.20309
0.92936	0.197966	-0.19797
0.93436	0.19268	-0.19268



APPENDIX B  
SIMULATOR SAFETY AND STARTUP DOCUMENTATION

**General safety warnings and precautions:**

1. Safety is the first priority.
2. The simulator emits extremely high levels of thermal radiations that can cause severe burns and even fatal injuries.
3. Highly concentrated thermal radiations may ignite objects and cause fires.
4. The Xenon arc lamps are pressurized and may shatter, particularly during startup and shutdown. Glass splinters may cause severe injuries.
5. Always wear safety glasses and protective clothing when the simulator shutter is open.
6. The simulator operates at extremely high, potentially fatal, electrical power levels.
7. Always think before your act.
8. If in doubt, turn off the simulator. Know where the off switch is.
9. Know where the fire extinguisher is.
10. Know how to operate a fire extinguisher.
11. Always watch the experiment.
12. Two properly instructed persons have to be present during an experiment.
13. No person is allowed inside the simulator room when the simulator is powered up, unless Dr. Petrasch is present and authorizes maintenance operations.
14. Use Plexiglass shields and close windows to the control room.

**Startup checklist:**

1. Turn on flux mapping system (computer labeled “FLUX MAPPING”, start Matlab, start ‘flux.m’).
2. Turn on simulator control DAQ (computer labeled “DAQ”, start LabView, run program). Make sure all lamps are shut off in the program.
3. Wear protective clothing when simulator shutter is open; welding jacket, long trousers, and safety glasses.
4. Uncover mirrors.
5. Close simulator shutter.
6. Check experiment; cover up exposed parts with Zirconia felt or Aluminum foil.
7. Position experiment and check position with mounted laser levels.
8. Turn on experiment DAQ.
9. Turn on cooling water.
10. Turn on the back door fan.
11. Turn on power to rectifiers (7 switches in the gray enclosure in the simulator room, switch on separately leaving 1 second in-between each).
12. Close all doors to the simulator room.
13. Warn people in the shop and control room.
14. Make sure nobody is inside the simulator room.
15. Turn on lamp fans.
16. Open shutter.
17. Put on welding goggles.
18. Turn on main switch.

19. Turn on simulator in DAQ.

20. Carefully watch the experiment.

**Shutdown checklist:**

1. Turn off the simulator in the DAQ.

2. Turn off the main switch.

3. Wait until shutter is completely closed.

4. Wear protective clothing and safety glasses.

5. Inspect experiment for fire or embers.

6. Wait 15 minutes for lamps to cool down.

7. Turn off all lamp fans.

8. Turn off power to rectifiers (7 switches in gray enclosure).

9. Turn off cooling water.

10. Open the shutter.

11. Cover the mirrors (wear protective clothing and safety mask).

12. Close shutter.

13. Turn off back door fan.

APPENDIX C  
PERIPHERAL SYSTEM DOCUMENTS

**VXM Movement Instructions**

- Motor 1 moves the XY table toward (negative move) and away from (positive move) the control room (i.e. along the focal plane)
  - Motor 2 moves the XY table towards (positive move) and away from (negative move) the simulator (i.e. in and out of the focal plane)
1. Send the XY table to both positive limit switches
    - a. Motor 1 command: F C I1M0, R
    - b. Motor 2 command: F C I2M0, R
  2. Return to the pre-defined location (previously measured by incrementing the XY table from the terminal)
    - a. Motor 1 command: F C I1M-7800, R
    - b. Motor 2 command: F C I2M-17500, R
    - c. Replace the number values 7800 and 17500 with the measured values pertaining to your setup

Note: Do not use the number pad to enter numbers or symbols, it will result in a double keystroke value being placed at the end of the command line

**Flux mapping system documentation**

Start program in MATLAB: flux.m

Program window must be on top. Program is controlled by keystrokes.

A: Adjust colorscale to current min and max.

D: Deskew. Use R or L prior to using D.

G: Switch display output to gray level.

J: Switch display output to color.

K: Turn off Deskew mode (kill).

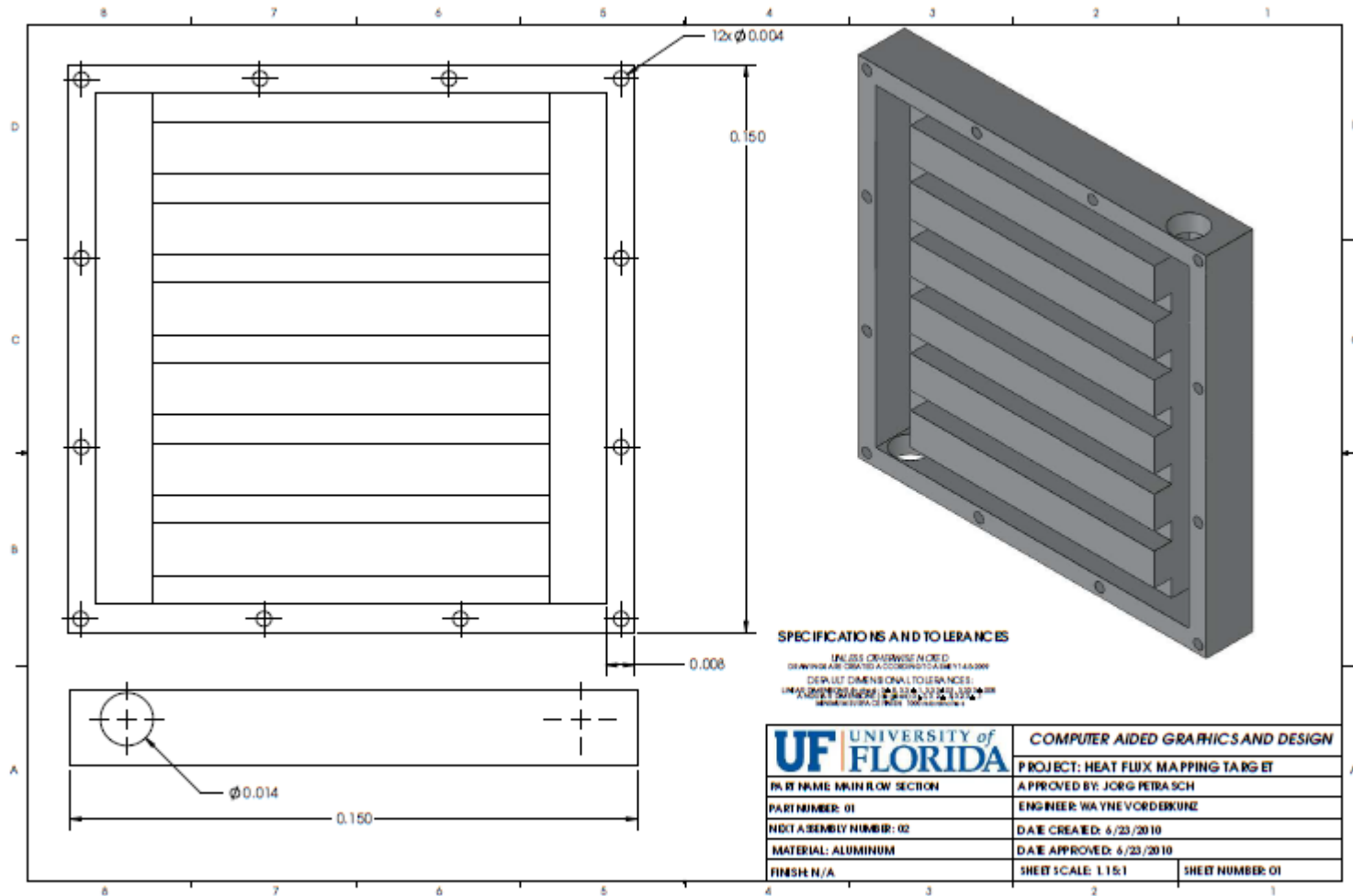
L: Load predefined reference square.

O: Turn image adjust off.

Q: Quit program. Always use Q, never just close the program window, since the connection to the camera is left open and flux can only be restarted after closing and reopening MATLAB.

R: Define reference square by clicking on image. This should be done before using D.

S: current image is saved as png: raw and adjusted. If this is the first time S is hit since the program has been started a new directory with respective date and time is created.



SolidWorks Educational License  
 Instructional Use Only

## Certificate of Calibration

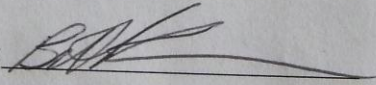
Customer:	University Of Florida
Model Number:	TG2000-73
Serial Number:	9304
Date Calibrated:	03-31-2011
Recalibration Due Date:	03-31-2012

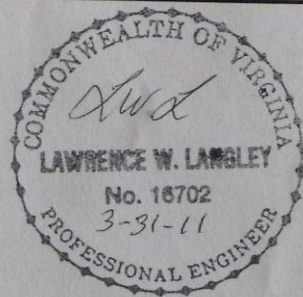
### Thermogage Circular Foil Heat Flux Transducer

Sensor Scale Factor*:	43.357 W / cm <sup>2</sup> / mV
Sensor Sensitivity*:	0.023 mV / W / cm <sup>2</sup>
Heat Flux Sensor Calibrated At:	0 - 650 W / cm <sup>2</sup>
Sensor Coating:	Colloidal Graphite
Reference Pyrometer:	7000-1 #8; Cert.#PC1027

\* Scale factor and sensitivity are for incident heat flux. Sensor emissivity is 0.82. The scale factor is the reciprocal of the sensitivity; both are provided here for convenience.

These calibrations were performed using instruments whose accuracy is traceable to the National Institute of Standards and Technology (NIST) and following procedures set in the Vatell Quality Assurance Manual.

Calibrated by: 



## LIST OF REFERENCES

- [1] Erbs, D. G., Klein, S. A., and Duffie, J. A., 1982, "Estimation of the diffuse radiation fraction for hourly, daily and monthly-average global radiation," *Sol. Energy*, **28**, pp. 293–302.
- [2] Hirsch, D., Zedtwitz, P. v., Osinga, T., Kinamore, J., and Steinfeld, A., 2003, "A New 75 kW High-Flux Solar Simulator for High-Temperature Thermal and Thermochemical Research," *J. of Sol. Energy Eng.*, **125**, pp. 117-131.
- [3] Zekai, Ş., 2004, "Solar energy in progress and future research trends," *Prog. in Energy and Combust. Sci.*, **30**, pp. 367–416.
- [4] Liu, B. Y. and Jordan, R. C., 1963, "Rational procedure for predicting the long-term average performance of flat-plate solar-energy collectors with design data for the US, its outlying possessions and Canada," *Sol. Energy*, **7**, pp. 53-74.
- [5] Duffie, J. A. and Beckman, W. A., 1974, *Solar energy thermal processes*, Wiley, New York.
- [6] Price, H., Lupfert, E., Kearney, D., Zarza, E., Cohen, G., Gee, R., and Mahoney, R., 2002, "Advances in Parabolic Trough Solar Power Technology," *J. Sol. Energy Eng.*, **124**, pp. 109–125.
- [7] Thomas, A. and Guven, H., 1993, "Parabolic trough concentrators—design, construction and evaluation," *Energy Conv. and Manag.*, **34**, pp. 401–416.
- [8] Friedman, R. P., Gordon, J. M., and Ries, H., 1993, "New high-flux two-stage optical designs for parabolic solar concentrators," *Sol. Energy*, **51**, pp. 317–325.
- [9] Mills, D., 2004, "Advances in solar thermal electricity technology," *Sol. Energy*, **76**, pp. 19–31.
- [10] Kongtragool, B. and Wongwises, S., 2003, "A review of solar-powered Stirling engines and low temperature differential Stirling engines," *Renew. and Sust. Energy Rev.*, **7**, pp. 131–154.
- [11] Kaushika, N.D, 1993, "Viability aspects of paraboloidal dish solar collector systems," *Renew. Energy*, **3**, pp. 787–793.
- [12] Baker, A. F., Faas, S. E., Radosevich, L. G., Skinrod, A. C., Peire, J., Castro, M., and Presa, J. L., 1989, "US-Spain evaluation of the Solar One and CESA-I receiver and storage systems," Sandia National Labs.
- [13] Romero, M., Buck, R., and Pacheco, J. E., 2002, "An Update on Solar Central Receiver Systems, Projects, and Technologies," *J. Sol. Energy Eng.*, **124**, pp. 98–108.

- [14] Petrasch, J., Coray, P., Meier, A., Brack, M., Haberling, P., Wuillemin, D., and Steinfeld, A., 2007, "A Novel 50 kW 11,000 suns High-Flux Solar Simulator Based on an Array of Xenon Arc Lamps," *J. Sol. Energy Eng.*, **129**, pp. 405–411.
- [15] Sayre, R. M., Cole, C., Billhimer, W., and Stanfield, J., 1990, "Spectral comparison of solar simulators and sunlight.," *Photodermatology, Photoimmunology & Photomedicine*, **7**, pp. 159-165.
- [16] Govaerts, Y. M. and Verstraete, M. M., 1998, "Raytran: a Monte Carlo ray-tracing model to compute light scattering in three-dimensional heterogeneous media," *IEEE Trans. on Geosci. and Remote Sensing*, **36**, pp. 493–505.
- [17] Lai, B. and Cerrina, F., 1986, "SHADOW: A synchrotron radiation ray tracing program," *Nuc. Inst. and Meth. in Phys. Res. Section A: Accelerators, Spectrometers, Detectors and Assoc. Equip.*, **246**, pp. 337–341.
- [18] Cashwell, E. D. and Everett, C. J., 1959, *A practical manual on the Monte Carlo method for random walk problems*, Pergamon Press.
- [19] Jacoboni, C. and Reggiani, L., 1983, "The Monte Carlo method for the solution of charge transport in semiconductors with applications to covalent materials," *Rev. Mod. Phys.*, **55**, pp. 645–705.
- [20] Modest, M. F., 2003, *Radiative heat transfer*. Academic Press, San Diego.
- [21] Hammersley, J. M. and Handscomb, D. C., 1975, *Monte Carlo methods*, Methuen, London.
- [22] Shreïder, I. A., 1964, *Method of statistical testing: Monte Carlo method*, Elsevier Pub. Co., Amsterdam.
- [23] Petrasch, J., 2010, "A Free and Open Source Monte Carlo Ray Tracing Program for Concentrating Solar Energy Research," *ASME Conf. Proc.*, **2010**, pp. 125–132.
- [24] Ulmer, S., Reinalter, W., Heller, P., Lüpfer, E., and Martinez, D., 2002, "Beam characterization and improvement with a flux mapping system for dish concentrators," *J. of Sol. Energy Eng.*, **124**, pp. 182-188.
- [25] Geyer, M., Lüpfer, E., Osuna, R., Esteban, A., Schiel, W., Schweitzer, A., Zarza, E., Nava, P., Langenkamp, J., and Mandelberg, E., 2002, "EUROTROUGH-Parabolic trough collector developed for cost efficient solar power generation," in *11th Int. Sym. on Conc. Sol. Power and Chem. Energy Tech.*, pp. 04–06.
- [26] Fernández-García, A., Zarza, E., Valenzuela, L., and Pérez, M., 2010, "Parabolic-trough solar collectors and their applications," *Renew. and Sust. Energy Rev.*, **14**, pp. 1695–1721.

- [27] Steinfeld, A., Brack, M., Meier, A., Weidenkaff, A., and Wuillemmin, D., 1998, "A solar chemical reactor for co-production of zinc and synthesis gas," *Energy*, **23**, pp. 803–814.
- [28] Z'Graggen, A., Haueter, P., Trommer, D., Romero, M., De Jesus, J., and Steinfeld, A., 2006, "Hydrogen production by steam-gasification of petroleum coke using concentrated solar power—II Reactor design, testing, and modeling," *Int. J. of Hyd. Energy*, **31**, pp. 797–811.
- [29] Cameron, C. P., 1993, "High heat flux engineering in solar energy applications," *Proc. of SPIE*, **1997**, pp. 460–471.
- [30] Kaluza, J. and Neumann, A., 2001, "Comparative Measurements of Different Solar Flux Gauge Types," *J. of Sol. Energy Eng.*, **123**, pp. 251-255.
- [31] Romero, V. J., 1991, "CIRCE2/DEKGEN2: A software package for facilitated optical analysis of 3-D distributed solar energy concentrators," User manual, *Sandia National Labs*.
- [32] Andraka, C. E., Yellowhair, J., and Iverson, B. D., 2010, "A Parametric Study of the Impact of Various Error Contributions on the Flux Distribution of a Solar Dish Concentrator," *ASME Conf. Proc.*, **2010**, pp. 565–580.
- [33] Jin, B. and Zheng, Y., 2006, "A meshless method for some inverse problems associated with the Helmholtz equation," *Computer Meth. in App. Mech. and Eng.*, **195**, pp. 2270–2288.
- [34] Li, H. and Yang, C., 1997, "A genetic algorithm for inverse radiation problems," *Int. J. of Heat and Mass Trans.*, **40**, pp. 1545–1549.
- [35] Colton, D. and Kirsch, A., 1996, "A simple method for solving inverse scattering problems in the resonance region," *Inverse Problems*, **12**, pp. 383-393.
- [36] Bleszynski, E., Bleszynski, M., and Jaroszewicz, T., 1996, "AIM: Adaptive integral method for solving large-scale electromagnetic scattering and radiation problems," *Radio Sci.*, **31**, pp. 1225–1251.
- [37] Ho, C. H. and Özişik, M. N., 1988, "Inverse radiation problems in inhomogeneous media," *J. of Quant. Spect. and Rad. Trans.*, **40**, pp. 553–560.
- [38] Subramaniam, S. and Menguc, M. P., 1991, "Solution of the inverse radiation problem for inhomogeneous and anisotropically scattering media using a Monte Carlo technique," *Int. J. of Heat and Mass Trans.*, **34**, pp. 253–266.
- [39] Park, H. M. and Yoon, T. Y., 2000, "Solution of the inverse radiation problem using a conjugate gradient method," *Int. J. of Heat and Mass Trans.*, **43**, pp. 1767–1776.

- [40] Golub, G. H., Hansen, P. C., and O’Leary, D. P., 1999, “Tikhonov Regularization and Total Least Squares,” *SIAM J. on Matrix Ana. and App.*, **21**, pp. 185-194.
- [41] Neumaier, A., 1998, “Solving ill-conditioned and singular linear systems: A tutorial on regularization,” *Siam Rev.*, **40**, pp. 636–666.

## BIOGRAPHICAL SKETCH

Ben Erickson was born in Cincinnati, Ohio in 1987. He attended Valparaiso University starting in 2006 and graduated with his Bachelor of Science in mechanical engineering in 2010. During his time at VU, Ben became heavily involved in both Alpha Phi Omega (a co-ed service fraternity) and Engineers Without Borders. Through his involvement in EWB he was able to help install water retrieval options such as a solar slow pump to help the locals in the Turkana region of northwest Kenya. Ben also became involved with the design and build of the solar furnace on the campus of VU which sparked his interest in renewable energy. He was accepted for graduate studies at the University of Florida and funded by Dr. Jörg Petrasch. His research consisted of the build of the solar simulator along with the design and installation of many of the peripheral systems. He graduated with his Master of Science in mechanical engineering in May 2012.